Progress in Aerospace Sciences 119 (2020) 100680

Contents lists available at ScienceDirect

Progress in Aerospace Sciences

journal homepage: http://www.elsevier.com/locate/paerosci

A review of installation effects of ultra-high bypass ratio engines

Andrea Magrini [a,*], Ernesto Benini [a], Hua-Dong Yao [b], Jos Postma [c], Chris Sheaf [d]

[a] Dipartimento di Ingegneria Industriale, Università Degli Studi di Padova, Via Venezia 1, 35131, Padova, Italy
[b] Department of Mechanics and Maritime Sciences, Chalmers University of Technology, SE-412 96, Gothenburg, Sweden
[c] DNW German-Dutch Wind Tunnels, Voorsterweg 31, 8316, PR Marknesse, the Netherlands
[d] Installation Aerodynamics, Rolls-Royce Plc., P.O. Box 31, Derby, DE24 8BJ, United Kingdom

ARTICLE INFO

Keywords:
Installation effect
Engine integration
UHBPR

ABSTRACT

The adoption of ultra-high bypass ratio (UHBPR) engines has been long recognised to bring about reduction of specific fuel consumption and noise emission. In the need to fulfil ambitious environmental targets and mitigate the aviation sector impact, they represent a smoother technology change, compared to futuristic aircraft designs featuring electric, distributed and boundary layer ingesting propulsion. However, the challenges related to UHBPR adoption can prevent a real system performance improvement, due to interdependent counteracting factors and enhanced interference between engine and airframe. This paper reviews the installation effects on underwing-mounted UHBPR turbofan engines, first presenting the cycle design studies and how they are affected by considering integration. The advancements in nacelle components modelling and optimisation are then reviewed, where new numerical models, statistical methods and optimisation algorithms are employed to tackle the inherently multi-objective problems. The computational estimation of installation effects and the studies on optimal engine position are also presented, highlighting the overall effect on the aerodynamic characteristics. Finally, the wind tunnel tests using powered engine simulators are discussed. The tools developed to quantify the thrust and drag figures of installed propulsors and obtain indications on their best underwing location now allow quite accurate estimations, both in numerical and experimental simulations. The higher level of interaction and the increased mutual sensitivity of engine operation and wing flow field, however, suggest the need to elaborate closely coupled methods to correctly replicate these effects and an assessment of current wind tunnel practices for the design and operation of powered engine simulators.

1. Introduction

The civil aviation market has seen an impressive growth since its birth in early '50s, with an outlook of further increasing the number of transported passengers by a factor of 7 by 2050 [1]. The scientific evolution of the relatively young flight science and the huge technological progresses in many other fields have led, in about seventy years, to a substantial improvement of noise, pollutant emissions and fuel consumption. The individual aircraft evolution, however, have been offset by the huge growth of the volume of flights, exacerbating the environmental impact of the aviation sector. In response to this overall negative trend, international institutions have set ambitious targets for its mitigation. In 2001, the European Commission ACARE 2020 vision [2] foresaw a 50% reduction in fuel-burn and noise, and 80% in take-off/landing NOx emissions, relative to year-2000 aircraft technology. Whilst these targets will not be achieved, a new FlightPath 2050 vision [3] has been released in 2011, requiring new limits of 75%, 65% and 90%, respectively, with the same term of comparison. The accomplishment of the new targets requires either technological step changes or novel aircraft paradigms.

Graham [4] summarised the new aircraft concepts proposed to achieve the requirements, which are based on alternative propulsion units, like open rotor, electric driven fans, boundary layer ingestion (BLI) propulsion, and change in traditional tube + wing configurations, like lifting fuselage frames with ducted engines, blended wing and laminar flying wing. In parallel to futuristic designs, a smoother change of current technology is also pursued, on a shorter-term basis. On the engine side, the evolution of propulsive units appears clear: the trend is leading towards the adoption of higher bypass ratio (BPR) turbofans, with increased values of the overall pressure ratio (OPR) and turbine

* Corresponding author.
E-mail addresses: andrea.magrini@unipd.it (A. Magrini), ernesto.benini@unipd.it (E. Benini), huadong.yao@cth.se (H.-D. Yao), jos.postma@dnw.aero (J. Postma), Christopher.Sheaf@rolls-royce.com (C. Sheaf).

https://doi.org/10.1016/j.paerosci.2020.100680
Received 30 June 2020; Received in revised form 9 October 2020; Accepted 10 October 2020

entry temperature (TET) [5]. It has been long recognised, in fact, that a higher BPR leads to improved propulsive efficiency, reduced noise and specific fuel consumption [6], while cycle thermal efficiency increases at larger pressure ratios and combustor chamber exit temperatures. Associated to very-high (VHBPR) and to ultra-high (UHBPR) bypass ratio values is the decrease in fan pressure ratio (FPR) and specific thrust. Engines featuring low specific thrust typically need more mass flow rate to be ingested and therefore larger fan diameters. The benefits related to propulsive efficiency and lower specific fuel consumption (SFC) brought about by high BPR are thus counterbalanced by increased nacelle drag, engine weight and enhanced installation effect caused by the propulsive unit.

As a result, although a typical increase of the fan diameter is generally beneficial to the uninstalled engine specific fuel consumption, the growth of nacelle drag and weight are detrimental to the aircraft performance. There is also likely to be a stronger aerodynamic coupling between the engine and the airframe. Overall, there is a risk that the gains in uninstalled engine performance are wholly or partly lost due to adverse engine-airframe installation and interference effects as well as additional nacelle weight [7]. The installation effect is traditionally quantified by the difference between the individual component performance in isolated condition and the performance after integration into the wing body [8]. Its phenomenology is due to alteration of pressure and velocity fields caused by the presence of nacelle, pylon and jet efflux from nozzles [9]. The gulley between nacelle and wing, for instance, creates a velocity jet causing suction peaks, vortex drag penalty and, in some cases, even shock-induced separation. Downstream of engine nozzle, the jet/free-flow interaction interferes as well with the wing pressure side, inducing viscous and profile drag. At off-design, additional interaction of the jets with the high-lift surfaces can reduce their effectiveness and augmented backpressure on nozzles affect their discharge ratios.

Hence, a number of problems are to be tackled to allow for full exploitation of UHBPR engines. On the internal side, operability, stability, and component matching require the adoption of additional subsystems, possibly with variable geometry. On the external side, bigger engines pose issues for drag and weight penalty and wing integration, both from the practical arrangement to guarantee sufficient clearance, and from the performance side, due to possibly enhanced mutual aerodynamic interference. In order to alleviate the potential obstacles hampering an effective achievement of noise reduction and efficiency gain, a change is required also in design approaches. Without a careful evaluation of system aspects, more traditional procedures based on sequential and decoupled design are likely to fail in finding a real working optimum. This encourages a tighter cooperation between the engineers working on different aspects of the air vehicles, as the sensitivity of engine operating conditions to the external flow field, and vice versa, is becoming more relevant. Following this, providing an overview of the currently available methods that are applied to design the nacelle components and to study the interactions between them and the airframe appears useful to promote the development of more integrated approaches for the design of UHBPR units.

This paper reviews the installation effects on UHBPR engines, with a focus on the aerodynamic aspects of standard aircraft configurations with underwing mounted nacelles. The review is conducted in terms of engine thermodynamic cycle design, nacelle aerodynamic design, numerical simulations and experimental approaches. The implication of having a UHBPR on the choice of key engine thermodynamic parameters are first assessed, by examining design studies considering advanced cycle configurations and novel technologies. The design tools used for nacelle intake, cowl and exhaust are also presented, highlighting the last advancements in numerical models and complex optimisation tools used to tackle multi-objective problems. Next, the computational methods employed for a more detailed analysis of the flow phenomena characterising the aerodynamics of engine integration and optimal nacelle positioning are reviewed. Finally, the experimental verification of powered engines is described and fundamental considerations for UHBPR tests are provided.

2. Installation effects on UHBPR engine design

The propulsive efficiency is defined as the ratio between the useful propulsive work and the kinetic energy of the jet. For a single stream propulsor it is expressed by the well-known Froude formula:

$$\eta_p = \frac{2V_0}{V_j + V_0} \tag{1}$$

where V_0 is the flight speed and V_j the jet speed. If the thrust can be expressed by $F_n = \dot{m}_j(V_j - V_0)$, by substitution in equation (1) one gets:

$$\eta_p = \frac{2V_0}{2V_0 + F_n/\dot{m}_j} \tag{2}$$

It is evident, therefore, that the propulsive efficiency is related to the specific thrust $F/\dot{m}_j$ and increases when the latter decreases. A reduction of specific thrust means that to keep the thrust level, the mass flow rate across the propulsor must be augmented, and the corresponding jet velocity reduced. In turbofan engines, this has been achieved by increasing the mass flow rate ingested by the fan and lowering its pressure ratio, leading to higher bypass ratio [5]. The adoption of high BPR, however, brings about a series of issues and challenges that were already clear when the possible benefits on system efficiency were first considered. Borradaile [10] effectively enlisted the difficulties associated to high BPR, low specific thrust units: conflicting requirements for nacelle design, reduced stability margin and inlet distortion for low FPR fan, fan-low pressure turbine coupling, reduced noise frequency and problematic integration of the powerplant. All these topics characterise the UHBPR turbofans and, as it will be shown throughout the review, they have pushed the scientific and industrial community towards the adoption of advanced design and analysis tools to implement remedies in each area.

The presence of counteracting factors that limit the effective utility of an unbounded increase in the BPR appears evident, when the aircraft is considered at system level. The low specific thrust and FPR are key parameters for determining the engine size, as they are generally achieved by increasing the fan and bypass duct size. The larger fan must rotate at lower speed, to produce the desired pressure ratio and keep the tip velocity within acceptable limits, related to supersonic compression performance, operability, aeromechanics, noise emission. This has a direct impact on the engine configuration, as the low pressure spool driving the fan, instead, would prefer high rotational speed to operate with sufficient efficiency and high specific work. Moreover, the increased power absorbed by the fan requires increasing low pressure turbine (LPT) diameter and its number of stages. At low LPT speed, in addition, the shaft thickness must grow to bear a high torque [7]. Zimbrick [11], comparing low BPR turbofan of early '90s with the advantages in Thrust Specific Fuel Consumption (TSFC) achievable by using UHBPR, described the chain of effects caused by low SFC units. Operating with a low FPR fan reduces the fan stability, because of the lower airflow velocities experienced by the fan and large operating line shifts from sea level to cruise. Adequate surge margin can require the adoption of variable area fan nozzles or variable pitch fan rotors [12], bringing additional weight and mechanical complexity. Dealing with large fan diameters also affects the size of the external nacelle, imposing more aggressive designs featuring larger diameter to length ratios. Therefore, in order to mitigate the impact of nacelle weight and drag, cowl length must be minimised. It is well known that the inlet must supply the fan with a sufficient mass flow rate throughout all the flight phases, with acceptable levels of distortion. A decrease of the intake length reduces the alleviation capability, increases the required lip contraction ratio, and limits the space for acoustic liners. Short length to diameter ratio are more likely to incur high wave drag penalties at cruise

and spillage drag is also enhanced for the large area capture ratio variation. The growth of by-pass nozzle external radius, constrained by boattail angle, furthermore, aggravates the weight of other subsystems, like the thrust reverser, for which alternative concepts might be required. Finally, the integration of the nacelle on wing airframe becomes more problematic and geometric constraints can reduce the extent of possible installation positions.

This picture delineates immediately a number of conflicting requirements associated to UHBPR engines, for which an optimal choice of the relevant parameters must consider several aspects at the same time, making the design more complex and interdependent. From the point of view of bulk engine variables, Fig. 1 shows how FPR, BPR and fan size are related to noise emission and fuel burn.

McKay [13] provided more quantitative indications on the relationship between BPR, FPR, OPR and thrust specific fuel consumption (TSFC) for a given turbine entry temperature and flight conditions, shown in Fig. 2. At increasing OPR, the BPR giving minimum TSFC is reduced, as well as the associated FPR. For OPR above 50, the theoretical optimal BPR would be above 40. This picture, however, does not consider the counterbalancing factors related to nacelle drag and engine weight, setting a likely lower value for BPR.

Including how the engine affects the aircraft at system performance and once it is integrated into the airframe leads to a different trend, highlighted in Fig. 3 (a) and (b), taken from Ref. [14]. Optimal bypass ratio minimising TSFC is expected to fall between 14 and 16 for a small class airplane, with a corresponding FPR as low as 1.3.

Guha [15] derived an explicit analytical equation linking the optimum fan pressure ratio to BPR, ambient conditions, specific thrust and efficiency of energy transfer between the core and bypass flow. The equation, validated against numerical optimisation using GasTurb software [16], shows a larger sensitivity to specific thrust and the existence of an optimum ratio between bypass and core exit velocities leading to minimum SFC and maximum specific thrust. For specific thrust in the range 15–20 lbf/(lb/s), the optimum FPR was claimed above 1.5 for BPR $>$ 8.

A number of studies in open literature were devoted to analysing possible engine configurations for UHBPR, aiming at estimating the best compromise solutions and technologies, needed to conciliate some of the requirements. For instance, a cure to fan-core incompatibility was found to be a geared connection between LPT and fan, leading to a geared turbofan architecture (GTA). A Rolls-Royce SNECMA M45SD-02 geared engine demonstrator was first run in the 1970 [17]. For regional applications, a geared architecture was adopted on the ALF502 engine for the BAe146. The technology was further studied for almost a decade by P&W in partnership with NASA, leading to the PurePower® Geared Turbofan™family. The PW1100G-JM, now powering the A320NEO class, features a BPR of 12.5 and a fan diameter of 81" or 2.054 m for a

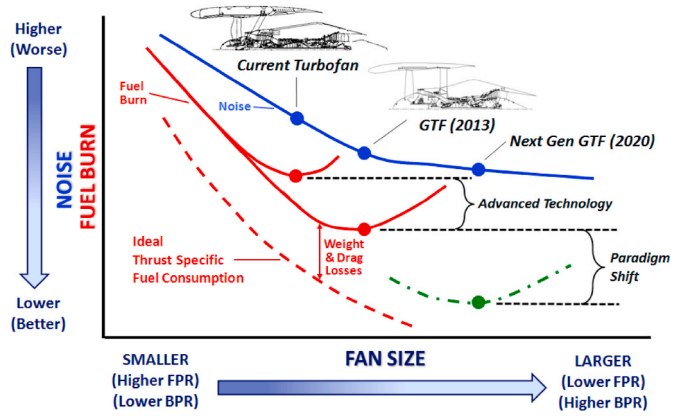

Fig. 1. Qualitative variation of noise emission and fuel consumption with FPR, BPR and associated fan diameter. From [5].

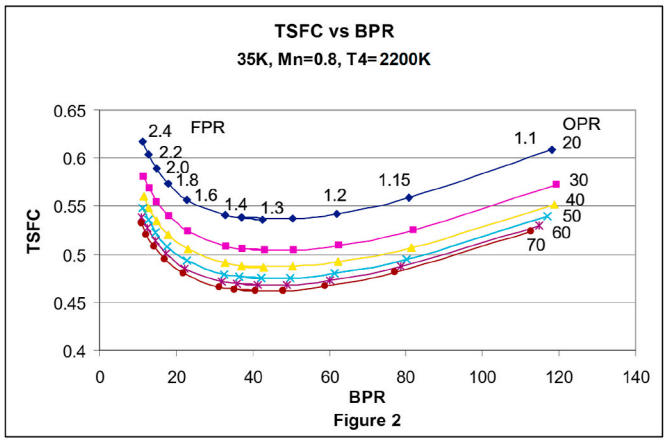

Fig. 2. Variation of TSFC vs BPR at given turbine inlet temperature and flight Mach number. From Ref. [13].

rated static thrust up to 150 kN or 33000 lbf [18]. For higher thrust long range widebody applications Rolls-Royce is currently developing innovative technology employing a geared connection between the fan and the intermediate pressure turbine. Fig. 4 illustrates the technologies embedded in the Rolls-Royce UltraFan® [19]. In addition to a geared architecture, also variable geometry components, alternative engine cycles and advanced combustion and thermal management contribute to the improvement of the propulsive unit efficiency. In the following section, the engine concepts cycle design proposed for future UHBPR are reviewed.

2.1. Engine concepts and cycle design

Based on the quantitative assessment methods of installation effects, different types of engines are conceptually designed. Christie [21] proposed a Propulsion System Integration Model (PSIMOD) for the engine cycle design with the installation effects. This model assesses the propulsion system integration and, furthermore, the overall flight characteristics and mission fuel burn. It also determines the engine requirements and the main aircraft characteristics at each point in the trajectory of a given mission in terms of the range, cruise altitudes, payloads and engine limitations. At each operation point, the engine cycle is adjusted to ensure that the thrust requirement is achieved. The fuel burn is then integrated over the mission. Engines with BPR from 5.1 to 11 for short and long haul applications are investigated, to highlight the impact of increased nacelle size and installation quality on the fuel burn.

Felder [22] investigated an electric distributed propulsion starting from Boeing N2 hybrid wing body, where superconducting generators, motors and transmission lines were used to transfer energy from the turbines to the fan. In this way, their motion is mechanically decoupled and they can operate at their optimal speed, virtually selecting a variable gear ratio throughout the flight, which is not possible with mechanical gear boxes. An extensive list of advantages brought by distributed hybrid electric propulsion is provided in the article, among which are a higher effective bypass ratio, lower power losses, high flexibility in positioning and operation, extended off-design compensation and capabilities in the event of engine failure, and reduced noise. For the case study, the turbogenerators were placed at the wing tips, exposed to freestream conditions, while a BLI continuous nacelle on the rear fuselage contained seven fan modules, featuring a FPR of 1.35 and a diameter of 50.6 in or 1.285 m. At the aerodynamic design point, the thrust was 17.570 kN and TSFC 13.27 g/(kN s). The effective BPR, the ratio of mass flow rate through all fans to rate through the engine core, was 19.2. The author reported the difficulty in estimating the flow state at the fan face, due to the fact that almost half of the height of the

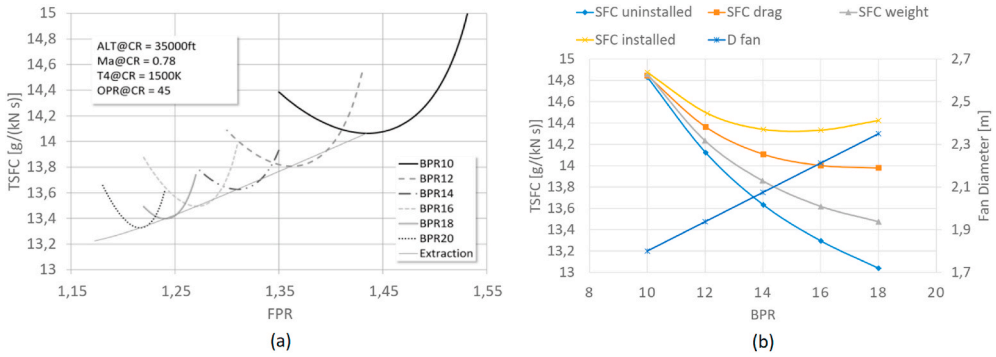

Fig. 3. Variation of TSFC with FPR (a) and with BPR (b) of installed engines. Adapted from Ref. [14].

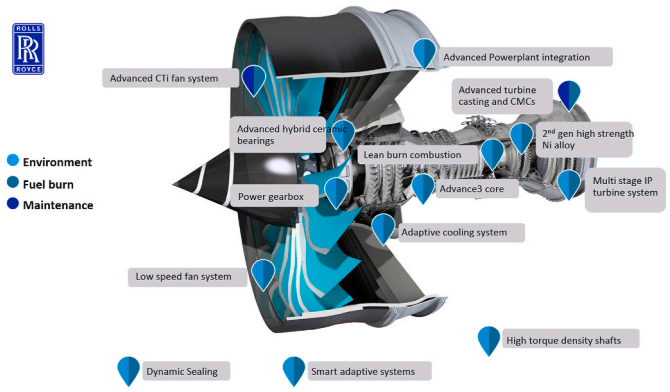

Fig. 4. Graphical representation of Rolls-Royce UltraFan® engine. From Refs. [20].

incoming flow was affected by boundary layer, making the thrust calculation using a standard approach for the inlet performance not appropriate.

Hall [23] summarised a series of activities for the design of an UHBPR turbofan for the Cambridge-MIT Silent Aircraft project, where noise was primarily tackled for a future aircraft concept. In the study, the off-design performance was considered from the beginning, as low noise requirement is more stringent far from cruise. The all-lifting-body baseline design belonged to the 250PAX class with 4000 nmi range. The flight mission profile was chosen to give the lowest maximum take-off weight (MTOW), as this was expected to minimise the radiated noise at take-off and approach. The engine location in the airframe was near the fuselage trailing edge, partially embedded and fed by an S-duct intake, to have good noise shielding and exploit BLI propulsion. At Top Of Climb (TOC), the selected UHBPR fan had a FPR of 1.40, with BPR of 16.8 for a SFC of 14.2 g/(kN s), resulting in a diameter of 2.16 m. Although lower FPR would be beneficial for noise target, minimising the extent of the variable area nozzle required, the sensitivity to the high level of inlet distortion would increase. The thermodynamic cycle was optimised to give minimum SFC and minimum fan diameter, fulfilling the derived thrust and noise requirements. From an architectural point of view, four engine configurations with three-spool, two-spool geared fan, two-spool geared fan with reduced fan speed and a single core driving multiple fans through mechanical connections were considered. This latter option, with four cores driving twelve fans, was thought to have advantages in terms of noise, as it would allow longer exhaust ducts to attenuate higher frequencies and more packaged units with less drag. A sensitivity study finally estimated that this unusual design could be much quieter than a four-engine podded configuration, offering a reduction of 5% in fuel consumption.

Larsson [24] conceptually designed a geared turbofan and a geared open rotor engines with Entry Into Service (EIS) in year 2020. A number of constraints regarding engine components, material limitations, shape factors, time between overhaul, runaway length, time to climb were considered for a short haul application with 150PAX and a range of 3000 nmi, with block fuel minimisation as a target. The geared fan BPR was 11.2 at mid-cruise, with FPR of 1.46 and fan diameter of 1.8 m. In contrast, the open rotor had a BPR of 87, FPR of 1.08 and propeller diameter of 4.2 m. In numerical simulations it achieved a 14% reduction of mid-cruise SFC, compared to the GTA, giving a 15% reduction in mission fuel burn. CO_2 and Nitrogen Oxides Emissions Index (EINOx) figures were similar for the two concepts. The direct operating cost (DOC) of the open rotor was reckoned 6% lower than GTA, but the datum was sensitive to the fluctuations of fuel price and referred to the price value of that time.

Kestner [25] analysed engine sizing for two concepts that were expected to represent 2020 standard (NASA N+2 time frame): an advanced direct drive turbofan (DDTF) and a geared turbofan. By surveying the trend for OPR in the last 35 years, the author reckoned a conservative value of 46 to be achieved nowadays, thanks to improvement in materials, combustor architecture, cooling and machining. The reference case was selected as Boeing 777-200 ER with General Electric GE90-94B engines, featuring a BPR of 8.80, FPR of 1.58, engine diameter of 3.124 m. Using a multidisciplinary simulation tool developed by NASA, EDS, a general trend on noise margin versus fuel burn for two engine concepts was derived. In general, DDTF achieved better noise levels, while GTA better fuel burn. On a best compromise configuration, the GTA resulted to have FPR of 1.462, BPR of 15.10, engine diameter of 2.954 m, TSFC of 14.134 g/(kN s) and a gear ratio of 2.09. The DDTF counterpart had FPR = 1.492, BPR = 14.07, engine diameter of 2.944 m, TSFC = 14.259 g/(kN s). In contrast, the GE90-94B baseline had TSFC = 15.191 g/(kN s), with an engine diameter equal to 3.1242 m. The trend derived was in agreement with general observation that specific thrust decreases with FPR, leading to larger diameters and higher nacelle drag and engine weight, *de facto* setting an optimum value for BPR.

In addition to geared turbofan, other technologies have been proposed for high BPR engines. Krishnan [12] compared the relative merits of two future architecture with GTA, a variable area nozzle (VAN) and a variable-pitch fan (VPF). A VAN allows to adapt the engine operating point to different flight conditions and can be used to keep sufficient margin to surge line. However, its installation on UHBPR poses questions about the weight penalty. A VPF is conceived for the same purpose and could be more effective for UHBPR, for its placement near the axis is less sensitive to engine size. The baseline configuration had a BPR of 11.63, a FPR of 1.45, a gear ratio of 2.5, TSFC of 16.145 g/(kN s) with fan diameter of 1.872 m. The reference aircraft was a 150 PAX single-aisle Boeing 737-800. The study concluded that VPF becomes superior to VAN at BPR 20-27.

Aloyo [26] extended the previous analysis to a VAN GTA with nacelle-based thrust reverser and VHBPR, and a VPF with an aircraft-based thrust reverser. A preliminary performance study was conducted to size the vertical tail of a Boeing 737-300 like aircraft and

choose engine location compliant with geometric constraints, e.g. for ground and tyre distance, including weight of additional engine devices, like VAN and thrust reverser, which limit the engine size. After that, a FPR sweep from 1.2 to 1.8 at constant OPR of 46.301 was done to analyse relation between FPR and nacelle diameter, engine location, vertical tail area and fuel burn, among others. The study showed a minimum of fuel burn with a FPR around 1.5, and VPF attaining a lower minimum. With this value, the nacelle diameter was around 2 m. VPF was also studied at conceptual level by Yang [27], who used a 0D meanline code to assess the performance of an Ultra Fan engine, with BPR = 17.5, FPR = 1.33, OPR = 60, fan diameter 2.36 m. The author claims that pitch tuning offers a way of achieving the best efficiency and competitive SFC at different conditions, as well as an alternative throttling method combining stagger and rotational speed selection, leading to 1.5–2% improvement in cruise SFC.

Daggett [28] presented a 2003 NASA research on Ultra Efficient Engine Technology (UEET), addressed to assess the performance of three advanced General Electric (GE) and Pratt & Withney (P&W) powerplants on a technology study airplane. The study is unique in defining optimum fan diameters for high bypass ratio turbofan, targeting 2015-year UEET. A parent aircraft, Boeing 777-200 ER, with maximum take-off weight (MTOW) of 297556 kg, cruise speed of M = 0.84 and maximum range of 14250 km, was re-adapted with new optimised composite wing and baseline GE90-94B and P&W PW4090 engines were resized to lower operating empty weight (OEW) and improved aerodynamics. Three UEET powerplants were then fitted onto the new baseline. The major difference between GE and P&W family was that the first featured an advanced direct drive counter-rotating fan, while the second had a geared fan on medium and big engine, the latter with VAN and advanced technology nacelle (ATN) using active flow control at lip and core-mounted thrust reverser. Details of the three configurations per type are summarised in Table 1. The UEET engine integration into the baseline airframe required some iterations to obtain optimal configurations, where changes affected both engine size and airframe. The final configurations were then compared to the baseline, to draw indications on engine giving the lowest block fuel consumption for a typical mission or a cost indicator, CAROC, including trip fuel costs, crew, maintenance, landing fees, ground handling, communications, ground power and overhead. For the P&W family, the optimal engine for fuel burn and cost was the medium STF1173, having a 15.79% reduction of block fuel use compared to the baseline aircraft. An equal outcome was found for GE family, with best fuel and cost engine laying between medium and large, at BPR around 11. In absolute terms, the cost indicator resulted similar for optimal engines of both families. The analysis was finally extended to different aircraft sizes: a small (162 seat, 10886 kg thrust) and a big (large 403 seat, 54431 kg thrust, low wing, twin engine). Among the three engines considered for both planes, the medium one appeared to be the best suited for the same previous criteria. In the small aircraft, BPR was 14.3 with an approximate fan diameter of 1.735 m, while in the big aircraft to the same BPR corresponded an approximate diameter of 3.604 m. The summary of the project results are represented in Fig. 5.

Bijewitz [29] presented a similar study of two evolutionary improved UHBPR turbofan engines for an entry-into-service of year 2035+, for a medium to long range advanced aircraft of 340PAX. One engine has a three-spool Direct Drive Turbofan (DDTF), whereas the other with a Geared Turbofan (GTA) (see Fig. 2). A detailed study of propulsive system architecture using an engine simulator was provided, similarly to Ref. [28]. They evaluated isolated propulsion system performance in terms of specific fuel consumption (SFC) for a broad range of design bypass ratio. In order to additionally capture the effects of the propulsion system weight and drag on the fuel burn optimum design values of BPR, a trade-factor based study was conducted. It is found that the optimum BPR and the relative improvement potential are dependent on the assumptions of the technology level, the associated component efficiencies, the block fuel exchange rates for SFC, and the drag and weight. Apart from the fuel burn improvement potential, the fan size and specific thrust levels might also be dictated by the noise targets, which lead to the designs that do not necessarily coincide with the fuel burn optimum ones. For DDTF, the SFC was found to be strongly sensitive to number of LPT stages, as this is directly related to stage loading and efficiency, whereas GTA showed continuous decrease of SFC in the range of BPR examined. The summary of selected design configurations for the two concepts is reported in Table 2. The choice was motivated by attainment of minimum SFC, despite for GTA given the relative flat curve near optimum BPR of 23, a BPR of 19.4 was selected, bringing to a reduction of nacelle weight and diameter with little loss of efficiency.

Berton [30] carried out an optimisation of engine independent design parameters for an aircraft of Boeing 737 class, including FPR, OPR, compressor work split, fan drive architecture (direct or geared), bypass nozzle type (fixed or variable-area) at a top-of-climb (TOC) condition of M = 0.80 at an altitude of 10668 m. FPR varied continuously between 1.35 and 1.70, whilst to settings for OPR were chosen as 32 (“low”) and 42 (“high”), the latter selected in order to have compressor exit annular passage height of half an inch, approximately. Aircraft system performance was assessed using a series of NASA codes for engine thermodynamic cycle (NPSS), aeromechanical design and weights (WATE), aircraft syntheses and sizing (FLOPS), aircraft weight (PDCYL), noise (ANOPP). The baseline aircraft was derived from Boeing 737-800 by an upgrade of expected future technologies (in 2015–2020 perspective), like composite frame, improved aerodynamics and UHB engines. The outcome of the study suggested that low ramp weight, there used as a cost indicator, can be minimised by high-FPR (1.70), high-OPR, direct-drive turbofan, which are more compact and lighter, compared to low-FPR (1.36), high-OPR, geared turbofan, resulting in lower block fuel use. A best compromise solution for block fuel and ramp weight was also found, having a FPR of 1.48, gear-driven fan, OPR of 42 and fixed area nozzle.

In a follow-up analysis [31], the authors partially revised some of the assumptions of the first research, such as the thrust requirement was set at sea level and M = 0.25, BPR was calculated assuming jet velocity ratio of 1.6, loss models better accounted for engine architecture, LPT cooling was permitted. Two engine classes called “low work” and “high work” were defined, as regards the work split between LP and HP compressor, the former having lower pressure rise across LPC. OPR was fixed to 42 and a range of FPR was investigated for three configurations: direct-drive low-work, direct-drive high-work, and high-work geared--drive. Fig. 6 (a) shows the obtained relation between FPR and BPR for these three families, while Fig. 6 (b) illustrates the variation of TSFC vs FPR. Dotted lines connect to configurations for which design ground rulers leads to practicality issues, and shaded lines are referred to previous analyses of [30]. Indeed, as FPR is decreased, BPR rapidly increases and the associated larger nacelle diameter (for GTA, it was 2.316 m at FPR = 1.5 and 2.835 at FPR = 1.3) makes more difficult to accommodate the engine under the wing, only acting on landing gear height and without wing shearing. The relationship between TSFC and FPR is almost linear and the variation of TSFC is around 11% when FPR is reduced from 1.7 to 1.3.

In terms of aircraft system, the outcome of the first study was

Table 1
Data for GE UEET engines [28].

Engine Label	Baseline GE90-94B	GE58-F2 B7	GE58-F2 B6	GE58-F2 B5
Fan Diam. [m]	3.124	2.552	2.758	3.137
BPR	7.8	7.43	9.47	13.1
FPR Design	1.46	1.8	1.65	1.45
Nacelle L/D	–	1.58	1.56	1.42
Engine Label	Baseline PW4090	STF1171	STF1173	STF1174
Fan Diam. [m]	2.868	3.010	3.249	3.777
BPR	6.2	11.5	14.3	21.5
FPR Design	1.6	1.55	1.45	1.32
Nacelle L/D	–	1.25	1.25	1.10

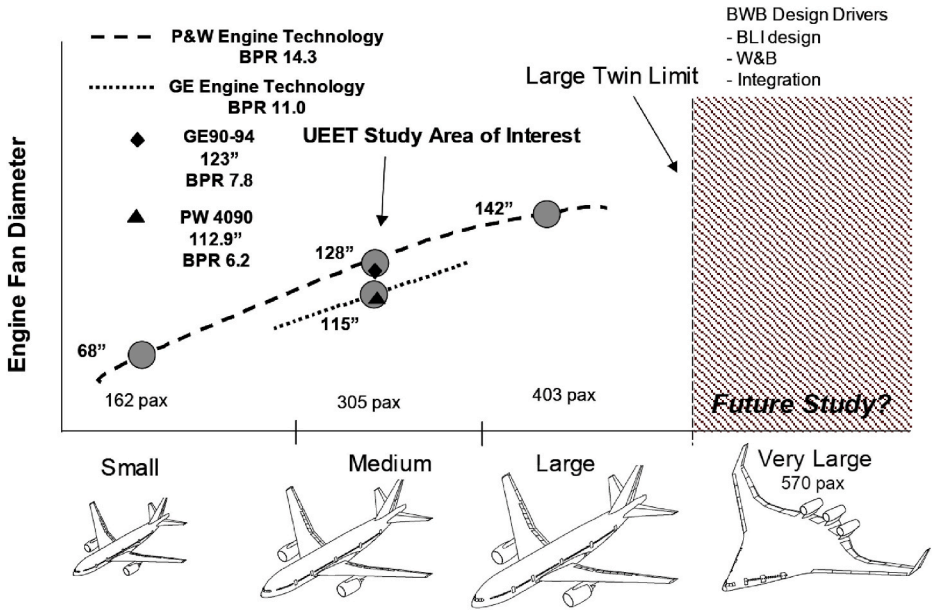

Fig. 5. Summary of result of optimal engine selection for UEET NASA study. From Ref. [28].

Table 2
Summary of selected configurations for 2035+ UHBPR engines of 340PAX aircraft.

Parameter	DDTF	GTA	Δ [%]
Engine Size			
Fan Inlet Diameter [m]	2.79	3.35	20.1
Max. Climb Point			
Operating Condition	M = 0.78, FL350, ISA		
Fn [kN]	56		
BPR	13	19.4	49.2
F_N/W2 [m/s]	119.7	83	−30.7
OPR [−]	60		
TET [K]	1750	1750	
Gear Ratio [−]	n/a	4.0	
SFC [g/s/kN]	13.29	12.67	−4.7
ΔSFC [%][a]	−20.1	−23.9	
η_c	0.607	0.609	14.2
η_c	0.843	0.826	−1.7
η_{pr} [−]	0.795	0.849	21.4
Integrated Characteristics			
Total PPS Weight [kg]	7774	7648	−1.6
Nacelle Wetted Area [m^2]	39.1	48.2	23.3
ΔBlock Fuel (rel. to GTA) [%]	5.5	0.0	
ΔBlock Fuel[a] [%]	−26.7	−32.2	

[a] (rel. to Year 2000 Technology). From [29].

confirmed in the trend. Low-work direct-drive engine with minimum block fuel had an FPR of 1.6 and BPR of 12.5, whereas minimum ramp weight was minimised with an FPR of 1.7 and BPR of 10.5, indicating a trade-off between maximum efficiency and minimum weight. A similar trend was found for high-work class, where lowest block fuel occurred for a geared, FPR = 1.5, BPR = 14.3 engine. The authors finally reported a direct comparison of all the configurations examined, showing the trade-off and the conflicting requirements. Although no single engine could simultaneously lead minimum block fuel, ramp weight, NO_x emission and noise level, the high-work geared turbofan with FPR = 1.5, BPR = 14.3, TSFC = 14.219 g/[kN s], diameter 2.316 m, had a very good balance, attaining minimum fuel use and only slight increase of weight and nitrogen oxides emission, with still more than 20% reduction in cumulative EPNL noise level, relative to 737-800 baseline.

Giesecke [32] carried out a thermodynamic and mechanical investigation of an over-wing UHBPR for a regional aircraft (CRC 800) of 100 PAX class with range from 2000 km to 2700 km and cruise at M = 0.78. The engine technology level was extrapolated for year 2025 and kept the same in the comparison of a BPR = 5 and a BPR = 17 geared turbofan, with a gear ratio of 3.3 and a FPR of 1.41. Table 3 illustrates the cycle design parameters for the TOC. The authors pointed out the benefits of a UHBPR for their configuration compared to low BPR, with a reduction of SFC of 18% at cruise condition. A VAN was also fitted to the larger engine, with area variation between −5% and +15%. The adoption of the variable are nozzle led to a better component matching and higher surge

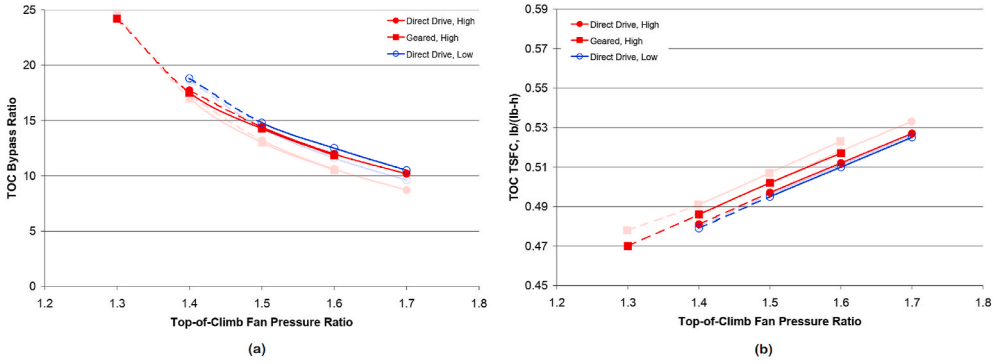

Fig. 6. Relation between FPR and BPR (a), and FPR and TSFC (b) obtained in Ref. [31] for engine sizing of an advanced single-aisle transport (ASAT).

Table 3
Comparison of engine cycle data for low (BPR5) and ultra-high (UHBPR17) bypass ratio engines. From Ref. [32].

Parameter	BPR5	UHBR17
BPR [−]	5	17
OPR [−]	36	70
TET [K]	1360	1750
FPR [−]	1.81	1.41
N1 [RPM]	5750	9234
N2 [RPM]	13788	18018
GR [−]	–	3.3
Nfan [−]	5750	2806
$\dot{m}_{total}$ [kg/s]	120.4	201.3
$\dot{m}_{bypass}$ [kg/s]	100.3	190.5
$\dot{m}_{core}$ [kg/s]	19.9	11.0
η_{core} [%]	51.8	56.9
η_{bypass} [%]	73.7	82.4
SFC [g/Ns]	16.31	13.26
Δ SFC [%]	–	−18.7

margin to the fan for certain operating points, reducing the fan noise up to 0.8 dB and the jet noise up to 2.2 dB. Compared to the fixed nozzle UHBPR engine with standard under-wing installation, the over-wing mounted VAN turbofan was claimed to bring an additional 1.7% reduction in fuel mass per mission and a 0.8% lower DOC.

The five-year EU FP7 project ENOVAL, ended in June 2018, addressed low pressure system of UHBPR (12-20), ultra-high OPR (50-70) engines, targeting CO_2 emissions in terms of fuel burn up to −5% and engine noise −1.3 EPNdB [33]. Three geared engines were sized for small to large aircraft and their main features are summarised in Table 4. The project analysed numerous components and aspects of modern turbofan, from low pressure ratio, low noise fan modules, including low pressure spool and power gear-box (PGB), to aeroacoustic technologies and components design, manufacturing and integration. Several experimental facilities and mock-up were used, in conjunction to advanced numerical methods. The wide number of topics examined and the results achieved, in terms of extension of technology readiness level (TRL) in many fields, are expected to have an important outcome in future engine systems.

This overview of recent research on high BPR turbofan has delineated the framework in which future jet engines will be developed and the major design drivers to pursue the stringent environmental requirements of 2050. From the complexity of the problem, it has been shown by various authors that simultaneous attainment of cost and emission indicators is likely to be possible only in a Pareto optimal sense, in a way that the best configuration depends on which aspect is considered predominant, given the constraints and difficulty in retrofitting a UHBPR on small/medium aircraft, without a partial redesign of the airframe.

Nonetheless, in order to provide some quantitative reference values, a summary of examined turbofan for a small airplane of 150/180 PAX class, like Boeing 737 or Airbus A320, is here reported in Table 5. These turbofan were conceived in different times (leftmost columns came first) and with a different technology level, expected to become feasible nowadays, apart from ENOVAL. Looking at BPR, it appears to fall in the range 14–16, which was also found on large aircraft throughout the review. The FPR instead varies between 1.45 and 1.55, whilst the ENOVAL small engine has a value of 1.36. Indeed, it embeds advanced future technologies at whole propulsive system, which were not considered in the other studies, making the comparison not completely balanced. The fan diameter is around 2 m, up to 2.32 m for the second column. Larger engines are expected to be more difficult to integrate on wing frame. The OPR, also indicative of core technology level, varies from a more conservative value of 42, to a more aggressive value of 74.3, with an average around 50.

For larger aircraft, of the 300PAX class, like Boeing 777–200 and Airbus A330, higher BPR can be more easily accommodated. A summary of reviewed research is reported in Table 6. The indications are in agreement with the previous ones, with scaled engine diameter now exceeding 3 m and the bypass in the range 14–16. According to Dagget [28], lowering FPR below 1.4 would result in further enlargement of fan size, and the increased nacelle weight and drag were found to offset the efficiency gain once the engine is installed.

The data of this summary can provide indications on variable ranges to the reader that is interested in developing representative UHBPR engine concepts. In fact, in many studies addressing the several aspects of high BPR, it is necessary to derive engine models first, to provide suitable boundary conditions. A clearer view of typical parameters found in the literature for a target aircraft class can be useful to compare new designs or circumscribe the design space. However, the presence of opposite influences on the overall performance sets an optimum BPR and FPR, that can be identified only by a thorough consideration of all associated effects. As suggested by Bijewitz [29], future methodology should consider more in detail the implications of UHBPR on whole aircraft sizing, including aerodynamic surfaces and additional subsystem weight, and optimal flight envelope.

Table 4
Reference engines for ENOVAL project [33].

	Small-Medium Turbofan	Large Turbofan	Very Large Turbofan
Thrust take-off [kN]	85.8	252	340
BPR (Mid Cruise)	16.2	16.2	16.0
FPR (Top of climb)	1.36	1.51	1.41
Configuration	1-Gear-3-8-2-3	1-Gear-4-11-2-4	1-Gear-3-9-2-4
Fan diameter [m]	2.03	3.17	3.84
OPR (Top of climb)	54.7	73.0	59.0
SFC (Mid Cruise) [g/kN/s]	13.98	13.73	13.47
Engine weight [kg]	4000	10136	11625
Gearbox max power [MW]	20.2	45.7	77.4

2.2. Nacelle design

Despite the complexity of all phenomena related to installation, the single components are typically first optimised for individual performance, allowing to apply established procedures in the decoupled design, where constraints other than aerodynamics can be more easily included. In particular, the design of the nacelle external cowl appears as a constrained problem where multiple operating conditions and geometric bounds must be considered [11]. Dagget [28] describes the main parameters defining the nacelle size. Among them, the overall length L_{nac} and maximum diameter D_{max} are the most important. The latter is set by fan size, clearance requirements and need to incorporate all surrounding subsystems. The former, instead, can be tuned by the designer and sets the aspect ratio. In principle, it should be minimised to reduce

Table 5
Summary of high BPR engines for a small 180PAX class aircraft examined in the report.

Parameter	Dagget [28]	Guynn [31]	Krishnan [12]	Aloyo [26]	ENOVAL [33]
FPR	1.45	1.5	1.55	1.5	1.36
BPR	14.3	14.3	–	–	16.2
OPR	74.3	42	51	46.3	54.7
Fan Diameter [m]	1.735	2.316	–	1.981	2.03
GTA	yes	yes	yes	yes	yes
VAN	no	no	yes	yes	yes
TSFC [g/kN/s]	–	14.219	–	–	13.98

Table 6
Summary of high BPR engines for a medium 300PAX class aircraft.

Parameter	Dagget [28]	Kestner [12]	ENOVAL [33]	Bijewitz [29]
FPR	1.45	1.462	1.51	–
BPR	14.3	15.1	16.2	19.4
OPR	74.3	46	45.7	60
Fan Diameter [m]	3.30	2.954	3.17	3.35
GTA	yes	yes	yes	yes
VAN	no	no	yes	no
TSFC [g/kN/s]	–	14.134	13.73	12.67

the wetted surface, contributing to friction drag, but low $L_{nac}/\ D_{max}$ nacelles tend to exhibit wave drag, due to high curvatures near the leading edge. An optimal trade-off exists, for which the total drag, the sum of wave and friction drag, is minimised. The metrics of interest for the cowl design include the drag at cruise condition (D_{cruise}), the drag rise Mach number (M_{DR}) and the spillage drag ($D_{spillage}$). The first parameter is obviously associated to the fuel consumption required at cruise and should be minimised. The second is usually defined as the derivative of drag coefficient with respect to freestream Mach number. The third one is the drag response to variation in Area Capture Ratio (ACR) of the intake, the ratio between the highlight and the ingested streamtube area infinite upstream $A_{highlight}/A_0$. This value is highly dependent on the engine working point and flight speed, and changes from around 0.75 at cruise to become greater than one at take-off and low speed flight. The multiple operating conditions and metrics naturally specify a multi-point and multi-objective problem that can be best addressed using CFD and optimisation algorithms.

Albert [34] presented a fully automatic procedure for nacelle and intake multi-point optimisation at cruise (M = 0.73), and static run (M = 0.05) for minimum peak Mach number. Explicit control on the maximum Mach number occurring in the external lip, in fact, limits the wave drag contribution. L_{nac}/D_{max} values were between 0.9 and 1.1 and geometric parameterisation used Class/Shape Transformation (CST) [35], B-Spline and Super-ellipse polynomial model (SP). The CST led to best results, with peak Mach numbers at cruise reduced up to 14% in the external cowl. Christie [36] adapted this promising technique to nacelle parameterisation. A generalisation of intuitive Class/Shape Transformation (iCST) was employed for use of explicit physical parameters in mathematical geometry definition, via a transformation matrix applied to the standard CST, which is a generalisation of Bézier curves and adopts Bernstein polynomials as basis. A series of analysis and optimisation for nacelle and intakes at incidence are reported. Robinson [37] used the tool to carry out multi-objective optimisation for a fixed length nacelle. The three aforementioned performance metrics were minimised for two UHBPR engine architectures, with BPR around 17.7 and two- or three-shaft configuration, at M = 0.85. Different nacelle length considered, for an advanced short and slim design with $L_{nac}/R_{HL} = 3.8$ and the two-shaft engine, the outcome revealed that larger drag rise Mach number, that is the Mach at which the C_D derivative exceeds 0.1, could be obtained at the cost of higher spillage drag.

Tejero [38] used the same framework addressing a similar problem. Eight intuitive design variables were used to represent the nacelle cowl and CFD solutions with the $\kappa - \omega$ *SST* turbulence model were employed to quantify the same metrics as before. The CFD model was first validated using data from axisymmetric cowls and an initial design space exploration was carried out for an aggressive short configuration with $L_{nac}/R_{HL} = 2.4$. Fig. 7 shows Mach number contours for three nacelle samples and the initial Pareto frontier. The impact of upper surface curvature appears evident on the Mach distribution, possibly causing shock waves and associated drag rise. In a subsequent Design Space Exploration (DSE), the range of L_{nac}/R_{HL} was extended from 2.4 to 3.0, with a total of 12 combinations of parameters describing the nacelle. The relative importance of the design variables was discussed and a feasible design space for each selected combination was individuated, providing general guidelines for shape factors of short and slim nacelles. The same author also reports a complex surrogate model with Gaussian Process Regression (GPR) based on the ordinary Kriging interpolation

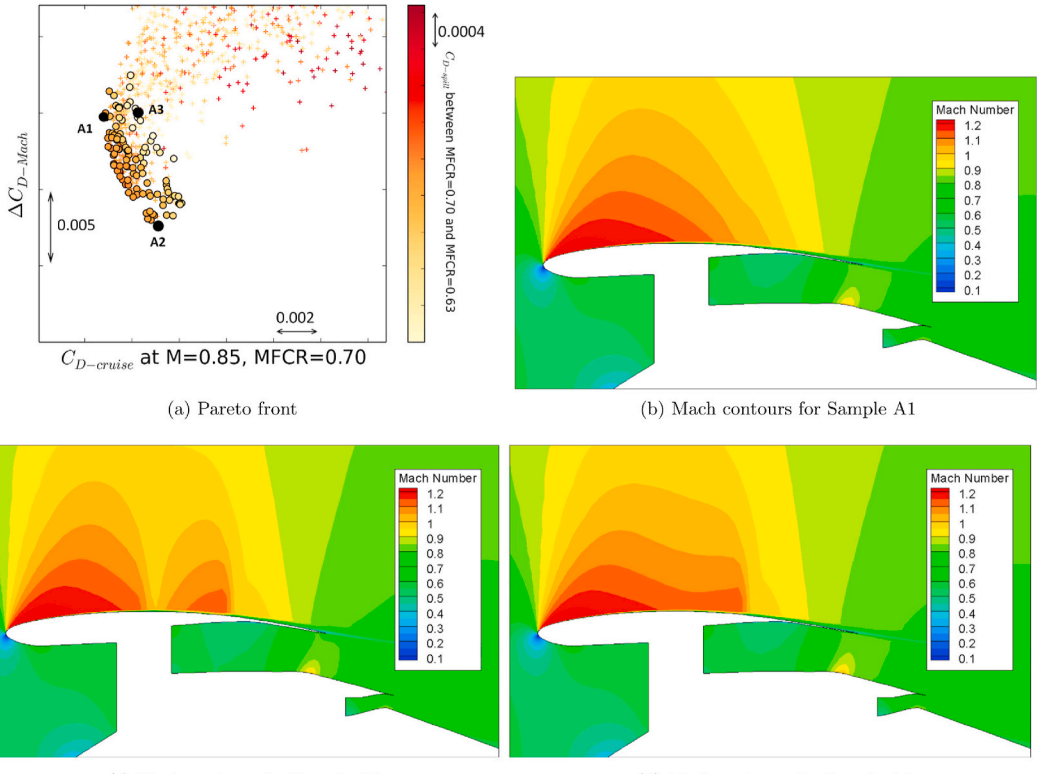

(a) Pareto front

(b) Mach contours for Sample A1

(c) Mach contours for Sample A2

(d) Mach contours for Sample A3

Fig. 7. Samples of short nacelle from initial exploration, with Pareto front and Mach number distribution. From Ref. [38].

method, using a quadratic regression function and an absolute exponential auto-correlation, that was adopted in order to improve and speed-up the convergence of the genetic algorithm, up to 25% compared to previous approach [39]. Fang [40] previously used the same combination of CST + Kriging for axisymmetric and 3D nacelle optimisation. Heiderbrecht improved Response-Surface Model (RSM) construction by exploiting data self-similarities and orthogonal properties [41]. The adoption of elaborated tools based on automatic shape optimisation, statistical analysis and meta-modelling appears, therefore, to have become a standard in the multi-objective constrained design of nacelles.

2.3. Intake design

In addition to studies on optimal external cowl shape, other nacelle components appear to be affected by installation effects and requiring additional attention. In advanced aircraft configurations, in fact, the complete coupling between the engine and the airframe exacerbates their interaction, posing several issues on the engine design and operation. The fan is the component most exposed to the external field distortions and even in standard underwing engine installation the reduction of FPR enhances the sensitivity to external pressure and incoming flow field, which during ground operation can present distortion levels pushing the fan towards its stability limit. Correct determination of fan-intake interaction is, therefore, essential to predict the effective working condition of a flying propulsive unit. Several computational and experimental studies have been devoted to analysing the problem, either focused on the external aerodynamic side, or on the fan operating point.

From an aerodynamic point, in fact, the intake must supply the engine with a clean flow with acceptable level of distortion throughout the entire envelope, while minimising external nacelle drag. The lip is the most critical location, as its design is a compromise between a slim shape with sharp leading edge, favouring the cruise, and a rounder shape with a thicker nose necessary at take-off to avoid separation and reduce distortion level. Similarly to the nacelle, the characteristic geometric parameter is the intake length to diameter ratio L_{int}/D. Typical designs exceed 0.55, while shorter intakes are sought to minimise the drag of the increased nacelle size. As L_{int}/D is reduced, the attenuation capability of incoming distortions is hampered, exposing the fan to operate closer to the stall point and to incur an efficiency drop. It is essential to capture the correct propagation of the fan effect and the distortion transfer through blade rows, in order to effectively design closely coupled fan/intake systems.

The flow field over an intake operating at incidence or crossflow is quite complex. The stagnation point moves well outside the highlight, causing a suction peak and a region of high Mach number, possibly resulting in a shock-wave, inducing a separation. Two vortices are formed in the lower lip, that are ingested by the fan. However, the rotor is able to keep its operating characteristics even in non-uniform conditions, inducing a flow redistribution to maintain a constant discharge condition, as long as the distortion is not too high to cause the blade stall [42]. Schulze [43] reported an extensive experimental investigation of scales dynamics of a stalled nacelle. A laminar separation bubble can form near the cowl leading edge, followed by a turbulent bubble just inside. The turbulent separation bubble is a highly unsteady phenomenon and gives rise to two counter-rotating vortices that are swallowed downstream by the rotor. The blade, therefore, sees a local change of incidence which can bring it closer to stall or induce aeromechanic excitation. Erbslöh [44] presented wind tunnel tests of nacelles at incidence, to study the potentials of energising boundary layer with air jets, to control separation. Oil flow visualization, depicted in Fig. 8, shows the complex flow pattern previously described, with a primary separation line marked S1, two focal points F, a secondary separation line S2, and a saddle point S. Experimental assessment of nacelle sensitivity to ground atmospheric gust, characteristic of take-off/landing conditions, was carried out by Übelacker [45], who showed that distortions have a

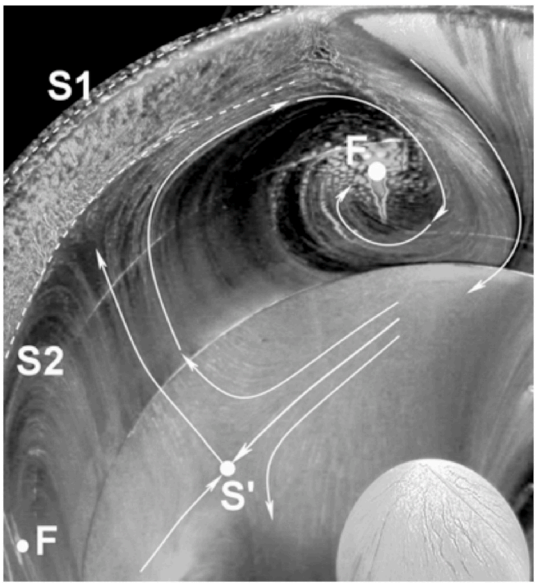

Fig. 8. Oil flow visualization of intake at incidence, showing separation lines and vortices. From Ref. [44].

critical effect on both attached and separated flow regime, changing the mean phase-locked flow and fluctuation velocities in the nacelle, potentially affecting fan stability.

The presence of the fan was found to cause an extension of separation-free operation and attenuation of distortion in the experimental campaign of Hodder [42]. Motycka [46] reported that the separation angle is Reynolds number and configuration dependent. Larkin [47] indicated that the extent of separation delay was 3°–4° relative to the flow-through case, based again on wind tunnel tests. Kennedy [48] studied the influence of fan modelling for CF34-3A turbofan engine, by comparing simulations with and without fan interaction with experimental data. The fan was confirmed to delay separation and reduce distortion level, causing a significant change in the path of ingested flow. Cao [49] carried out a systematic analysis of fan-intake interaction at different L_{int}/D ratios using a body force method, previously validated against uRANS. Confirming previous findings, at decreasing L_{int}/D the fan had the effect of either increasing the separation angle of attack or reducing the distortion level. At fan face, low sensitivity of separation level to L_{int}/D was reported. The suppression mechanism was attributed to the flow acceleration close to the casing caused by redistribution of the mass flow induced by the fan. This effect rapidly decays upstream of fan face, but is independent of L_{int}/D, explaining the constancy of reduction level and the lower sensitivity of fan presence for higher L_{int}/D. The separation delay was found to be 5 deg at $L_{int}/D = 0.17$, and zero for $L_{int}/D = 0.44$.

The European project ASPIRE, involving several research centres and Airbus, investigated design methods for advanced nacelles of future UHBRP engines, using low pressure ratio fan installed on a short cowl isolated nacelle, with $L_{int}/D \tilde{} 0.30$. Burlot [50] studied analysis methods with different fidelity, including low-order methods like actuator disk (AD) and body force model (BFM). The author concluded that a correct estimation of mass flow and fan pressure ratio can be obtained with simplified methods, but efficiency requires the use of full annulus unsteady simulation. Meheut [51] reported a code-to-code comparison between ONERA eLSA and DLR TAU and Trace for the same case, showing a good consistency. Stuerner [52] performed uRANS computation, assessing the influence of time step size on the resolution. The drag on the external nacelle surfaces was also found to be sensitive to modelling technique when operating at incidence, indicating that flow non-uniformities in the ingested streamtube might become relevant also for the force acting on the external cowl. Moreover, the unsuitability of

standard uniform engine boundary conditions to investigate specific intake states was remarked.

Schnell [14] summarised a series of activities carried out at DLR related to short intakes and low pressure ratio fans. The V2500 two spool, FPR ~1.7, BPR = 4.8 turbofan, powering A320, was simulated with 60° total pressure inlet distortion and compared with an FPR = 1.35, BPR ~ 14 fan, designed at DLR and designated Fan135. As shown in other studies, the rotor blades crossing the distortion see an induced incidence that brings them operating closer to spill point, as shown in Fig. 9 left. A similar effect is viewed for low FPR fan, although the distorted characteristics are influenced in different ways. Sectors closer to the distortion boundary operate well beyond the steady-state stability margin, whilst for V2500 the local sector characteristics are less spread. More details of the comparison are provided in Ref. [53], where it is remarked that low FPR fan is subject to large variations of blade forces, which are challenging boundary conditions for the aeromechanic design. Furthermore, stronger incidence effects from the streamline curvature are observed and the distortion is propagated downstream with reduced attenuation, compared to high FPR fan.

Peters [54] describes a computational framework for the evaluation of short intake nacelles for low pressure ratio fans, using BFM and uRANS. The author discusses the design practice driven by competing requirements at cruise and off-design, which are also different from top to bottom sections. Assessment of nacelle drag and fan performance on three configurations, with L_{intake}/D of 0.50, 0.25 and 0.19 showed that the combined effect of external drag and fan efficiency decrease, at lowering L_{intake}/D, determines a non-monotonic trend of propulsive efficiency for L_{intake}/D between 0.25 and 0.50, suggesting the existence of an optimum inside this range. For $L_{intake}/D = 0.25$, the external drag was reduced by 16%, with an almost zero change in propulsive efficiency, relative to the standard cowl. Corroyer [55] presented a coupled fan/intake design optimisation with solid fan modelling using different numerical approaches, from Reynolds-Averaged Navier-Stokes (RANS) single passage to harmonic balance (HB) and uRANS. The optimisation focused on the intake shape but the objectives were the fan pressure ratio at take-off and its cruise efficiency, both found to be connected to the lip shape. The Fan135 was employed for the study, where crosswind, low speed and cruise were considered. In terms of numerical models, the simplest steady approaches were sufficient to capture the major flow features at incidence, but the unsteady content also responsible for fan performance degradation can be only obtained with time-accurate simulation, and partially with frequency-domain method. For the optimisation, a short intake with L_{intake}/D~0.34 was used, obtaining a 0.25% improvement of fan efficiency, but at the cost of slightly reduced take-off FPR, compared to the baseline long intake ($L_{intake}/D = 0.65$). This outcome indicated that the performance of shortened intake systems can be recovered with proper design.

The development of coupled design procedures is promoted by the investigations on future aircraft concepts, where the fan/intake interaction is present throughout the whole flight envelope. Yu [56] carried out CFD simulations of engine/airframe interaction for the BWB300 blended wing body, with two podded engines installed in the rearward of the fuselage, finding greater sensitivity at low speed and high incidence, but even at high speed the engine presence significantly changed the pressure field on the upper fuselage. Rodriguez [57] employed a multidisciplinary optimisation method for the design of a blended wing body engine intake, both for podded and BLI configurations. The engine fuel-burn rate was minimised by selecting a set of geometric design variables controlling intake shape or podded engine positioning. An engine performance simulator fed with CFD data provided the necessary objective function. Kim [58] tried to improve the engine/airframe coupling by using the engine simulator to provide boundary conditions at the discharge plane, as a function of fan face total pressure recovery. The intake of the NASA N2B hybrid wing body three embedded engines was then optimised using an adjoint solver, to reduce the drag by the elimination of a strong shock-induced separation first, and to minimise the distortion by reshaping the cowl diffuser, achieving a 12.5% reduction of distortion index. More recently, the same author published a similar study for N3-X hybrid wing body with sixteen fans in a mail-slot propulsor, modelled using a body force method [59]. The improved coupling compared well with full-annulus CFD simulations near the design point and allowed to replicate the fan effect consistently, far from choking, where BFM is known to suffer for transonic fans [60], allowing to optimise the cowl shape to reduce strong shock waves in the external part and decrease distortion levels.

In conclusion, similarly to the external cowl, the intake has to fulfil a series of conflicting requirements, but its impact on the overall performance is larger as it is directly coupled to the engine operation. For the novel short intake configurations that are needed to limit the drag and weight penalty of large nacelles and allow an effective adoption of large BPR turbofan, the boundary condition modelling becomes more important, especially at off-design. For the novel aircraft concepts with embedded engines, intake/engine coupling is simply unavoidable. The huge computational cost of time-accurate simulations needed for a precise study of the fan-airframe interaction, however, is not affordable to be used as the core design tool, even because it requires a detailed knowledge of the engine assembly, which might not be already available at that stage. As understanding the actual working point of the fan, the correct mass flow rate ingested and the efficiency are crucial for low FPR UHBPR propulsor operating with BLI, in the last years a number of reduced order models based on the body force approach have emerged [61]. Despite the need for further improvement [62], at current state they represent the most accurate way for fan-intake coupling that can be affordable in terms of computational resources.

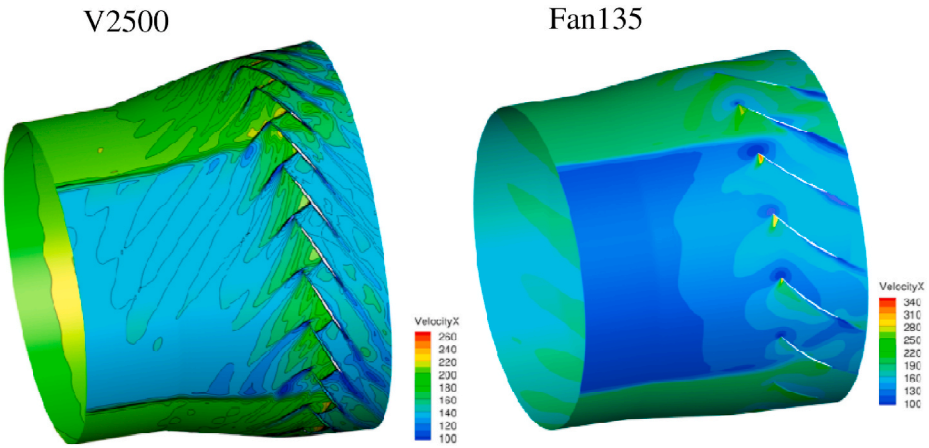

Fig. 9. Instantaneous Mach contour of full annulus uRANS for high FPR V2500 and low FPR Fan135 turbofan. From Ref. [14].

2.4. Exhaust design

Aft of the fan system is the exhaust system where the mass flow ingested by the engine is ejected into the free stream. The pressure forces acting on the exhaust surfaces are also affected by integration and determine a thrust variation that is either related to the sensitivity of nozzle operation to the discharge pressure, which occurs in the unchoked condition that can characterise UHBPR turbofans, and to the force on the nozzle cowls and afterbody, which is usually book-kept as a thrust component, falling within the streamtube [63]. The nozzle internal drag is about 1.5–2% of engine thrust, amounting to 15-20 drag counts. The scrubbing drag introduces an additional 0.3–0.9% thrust loss on high-bypass nacelles [64]. Moreover, as the BPR is increased, the ratio between the gross and the net thrust increases, given the larger ram drag associated to higher mass flow rate, enhancing the engine sensitivity to variations of gross thrust. It is, therefore, essential to derive design tools that are able to accurately capture the flow field of the jet exhaust and the forces there acting. Also in this field, the employment of high-fidelity CFD models and advanced tools for geometry parameterisation, design space exploration and data post-processing has become a common practice.

Zhang [65] pointed out the accuracy requirements for thrust estimation from nozzle simulation. The relevant performance metrics of a nozzle are its velocity coefficient C_V and its discharge coefficient C_{Disch}. The first one is defined as the ratio between the actual thrust and that produced by an isentropic expansion to freestream pressure. The second is related to the ratio between the actual mass flow rate and that of an isentropic nozzle. For a $C_V = 0.99$, a 0.1% uncertainty could cause a 10% error on the internal drag. The accuracy of CFD solutions of nozzle flows was tested and improved throughout a series of AIAA Propulsion Aerodynamic Workshops [66–69]. The European research (FP6) project called VITAL [70–73] was intended to present the characterisation of the installation effects for a typical high BPR engine using advanced numerical and measurement techniques. The third part of this project aimed to obtain a better understanding of the link between the jet flow and the noise generation, to validate the methods for computing the flow field and the noise sources for industrial configurations, and to assess the benefits of a serrated nozzle installed under a wing. Dezitter [71] assessed the CFD solvers for predicting the aerodynamic flows of different nozzles installed under the wing. The density gradient and compressibility corrections were introduced into the SST $\kappa - \omega$ turbulence model to better capture the physics related to high-speed hot jet flows. A high order discretization scheme and error estimation techniques were evaluated to increase the numerical accuracy. The CFD solvers were found appropriate for capturing the installation effects.

Goulos [74] presented an integrated framework for separate-jet nozzle design, called GEMINI, comprising a geometrical parameterisation module, stochastic methods for design space sampling, 0D models for engine thermodynamic analysis, CFD model for thrust and performance figures calculations, summarised in Fig. 10. The computational tool was first validated for a small TPS test case, with sufficient agreement. Subsequently, two engines representative of future architectures were considered, featuring a bypass of 16 and 11, respectively. The geometry of nozzle duct, core cowl and afterbody were varied using CST parameterisation, to find the sensitivity of performance metrics with respect to the physical dimensions and derive suitable design guidelines for the interdependencies of the eleven variables considered. In a subsequent study with the same engines [75], a response surface model based on Kriging interpolation was built from a DOE, showing an average reconstruction error of 0.567% for net thrust of the larger BPR = 16 engine. The RSM was employed for optimisation of overall velocity coefficient (core + bypass), reaching a 1.4% increase in net thrust for that turbofan. Analysis of the optimised shapes and design variables was found consistent with previously derived guidelines, proving the ability of the framework to identify the main mechanisms responsible for exhaust system aerodynamic performance. Giangaspero used Kriging and RBF models for generation of RSM of exhaust performance metrics, reaching estimated average errors within the accuracy found in literature relating CFD to nozzle experiments [76]. Goulous [77] also studied the influence of fan OGV exit flow radial profile on axisymmetric configurations, achieving improvements on the velocity coefficient up to 0.19% compared to uniform radial inflow, depending on the profile

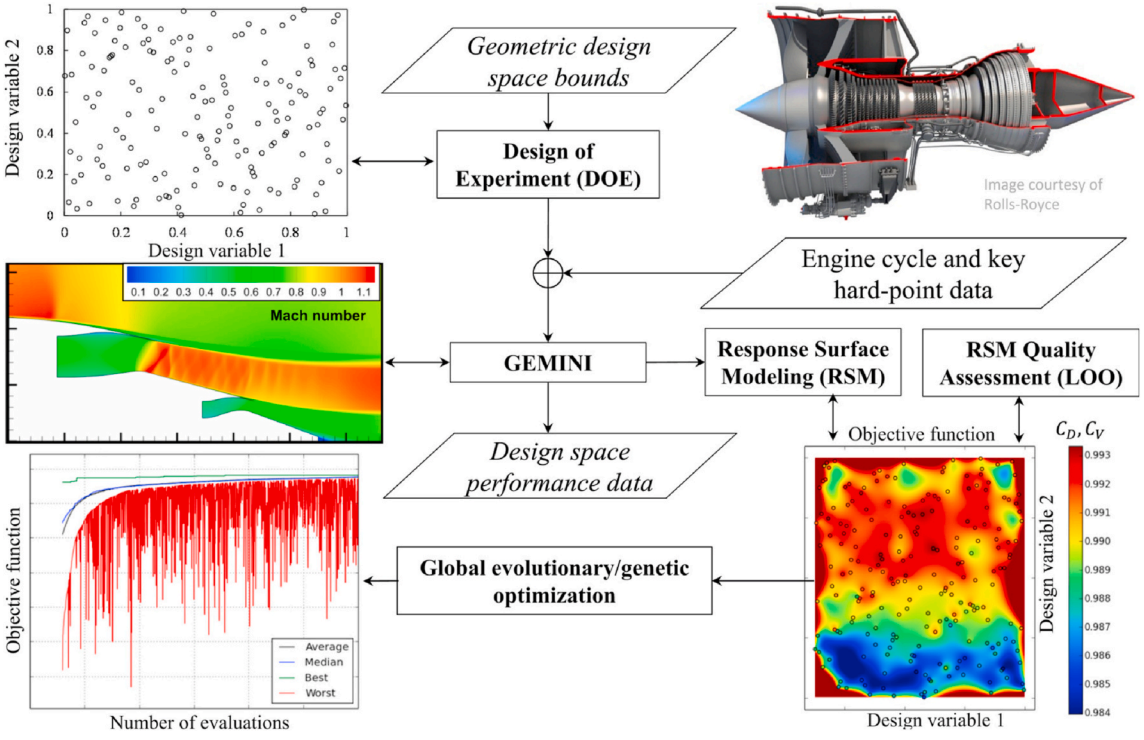

Fig. 10. Overview of the GEMINI framework for exhaust system design and optimisation. From Ref. [74].

distribution, which was also optimised in combination with the exhaust geometry.

Otter [78] studied the impact of non-axisymmetric exhaust lines on net propulsive force, obtaining variations from 0.12% to −0.28% relative to axisymmetric shapes. The best improvement was achieved with a 5% reduction of top and bottom line radius with respect to the sideline, as this gave rise to a reduction of post-exit streamline curvature and an increase of the favourable, i.e. thrust aligned, pressure force on the afterbody.

Wang [79] assessed the FNPR, CNPR and swirl angle influence on a nacelle system for a BPR 10 engine via CFD, finding a positive installation effect on nacelle drag due to increased pressure force on the exhaust cowls. Augmented FNPR and CNPR reduced the total drag coefficient up to 32.4%, when FNPR was changed from 2.2 to 2,6, whilst it was unfavourably affected by swirled flow exiting the fan stage.

Wang [80] performed LES on an UHBPR jet exiting from an isolated serrated nozzle, to predict near-field turbulence and far-field acoustics. Tyacke [81] continued the study in the installed case using LES-RANS, to produce a large high-fidelity validated aeroacoustic database of installed engines. Among other problems, indeed, noise generation is becoming a key area of technology improvement, with the constant enlargement of civil aviation volume, and it is another aspect influenced by mutual interaction of aircraft components.

3. Computational approaches for engine installation effect

In the previous sections, the main studies related to the design of UHBPR engines in terms of engine cycle and nacelle components have been reviewed, showing the progress made in the tools used for the design and analysis of complex subsystem, where a number of variables having an opposite influence on the individual performance is present. Notwithstanding the high level of accuracy reached by the computational models and the guidelines that can be derived using data reduction methods from statistical analysis, in the framework of UHBPR it is emerging a larger importance in the overall system performance, as gains in individual elements can be offset by losses caused by integration or deviation from nominal operating point. It is, therefore, mandatory to apply the same advanced tools used for the design of each component also for a more detailed evaluation of the interference generated in engine-airframe coupling. To this purpose, a careful examination of the flow phenomena characterising the aerodynamics of installed aeroengines can be carried out. Harris [82] reported a large number of effects brought about by installation. On the nacelle lip, the wing potential effect causes upwash and sidewash of the velocity field, changing the stagnation point position and the spillage drag, consequently. On the rear part of the cowl, the wing circulation induces pressure gradients affecting the flow development. The pylon leading edge flow is also sensitive to wing flow redistribution, and in the inboard and outboard channel local supercritical regions can cause shock waves and detachment. The nacelle itself causes wing lift redistribution and change in pressure distribution, with shock-waves shift, modification of wave and lift-induced drag. On the exhaust, over-expanded fan jet flow can interact with nozzle cowl and afterbody surfaces, changing pressure and friction drag, with possible strong shock termination. In addition, the flow over the high-lift devices or additional nacelle subsystem, like thrust reverser, can interfere with the jet, either changing lift and drag, or inducing nozzle flow suppression and possible thrust modification.

3.1. Thrust/drag bookkeeping

The quantification of this complicated pattern of multiple effects can be performed with the aim of CFD tools, after a consistent thrust/drag bookkeeping (TDB) approach has been established. In a thrust/drag bookkeeping procedure, the forces acting on the powered vehicle are decomposed and attributed to the drag or to the thrust domain. Although this difference is somehow arbitrary, by convention the engine manufacturer takes care of everything occurring within the streamtube ingested by the propulsor, while the airframe engineer is competent at external flow. AGARD [63] and SAE [83] described in-flight thrust determination, reporting general principles for force decomposition that can be applied in numerical simulations as well as experimental testing. Fig. 11 shows the control volumes employed for thrust and drag calculation for a powered configuration. The balance between the thrust and drag domains can be used to determine the acting forces.

By using the impulse function $F_{Gi} = \dot{m}_i v_i + A_i(p_i - p_0)$ and setting $\varphi = \int[(p - p_0)\hat{n} + \bar{\tau}\cdot\hat{n}]\cdot d\mathbf{A}$ the force integral on a direction parallel to the freestream velocity, the quantities reported in Table 7, referred to Fig. 12, can be defined, according to a common scheme in the literature [63,83]. The core cowl, the core nozzle plug and the portion of the pylon scrubbed by the jet exhaust fall within the thrust domain and are accounted for as reduction of thrusts (indicated by θ), which are included in the modified gross thrust definition.

With a proper decomposition of forces established, their extraction from CFD simulations can be performed. There are two principal approaches to compute the drag, in particular, for a CFD solution. The first is called the near-field method and it involves the direct integration of the mechanical forces acting on a geometry, namely the pressure and viscous forces. Zhang [65] presented a TDB method for separated dual-flow nozzles of a turbofan, with focus on nozzle metrics. Christie [21] proposed a modified near-field TBD procedure to avoid interpolating forces on highlight plane and captured streamtube. Robinson [85] compared the approach with wake momentum loss from wind tunnel tests.

In contrast to near-field, which is a fast and direct method suitable for automatic drag extraction in DOE or optimisation, but suffers from data interpolation and numerical dissipation errors, there exist a second approach, called the far-field method, which is based on the law of conservation of momentum, formulated with variables in volume cells, e.g. Refs. [86] or, alternatively, on a survey plane located in far downstream wakes. Whilst in the near-field methods the drag components are the pressure and the viscous ones, in the latter several definition of drag forces are given, for instance:

- Viscous drag (irreversible): caused by the irreversible thermodynamic process of the loss in viscous boundary layers
- Wave drag (irreversible): caused by the irreversible process across shock waves
- Profile drag (irreversible): the sum of the viscous and wave drags
- Induced drag (reversible): caused by the reversible thermodynamic process of vortices in the wake

Fan [87] presented a review of these methods, among which several sub-approaches can be identified, relying on different physical quantities.

3.1.1. Isentropic wake-plane methods

The first concepts of far-field methods were based on isentropic wake-plane [88] and applied to assess aircraft profile drag in wind tunnel experiments. In contrast to the near field method that integrates the forces on the body surfaces, the far-field method by Betz is to formulate force integrals on a survey plane in the wake that is normal to the streamwise. The integral terms are associated with the total pressure loss and isentropic velocity. For an accurate drag estimation, the survey plan position is far from the body to align with the Trefftz plane, where viscous losses are negligible. This method is only valid for steady incompressible flow. The limit of Betz' method due to the Trefftz plane was resolved in Ref. [89]. In addition to the profile drag, an improved far-field method was proposed by Maskell to extract the induced drag and lift in the far downstream wake plane [90].

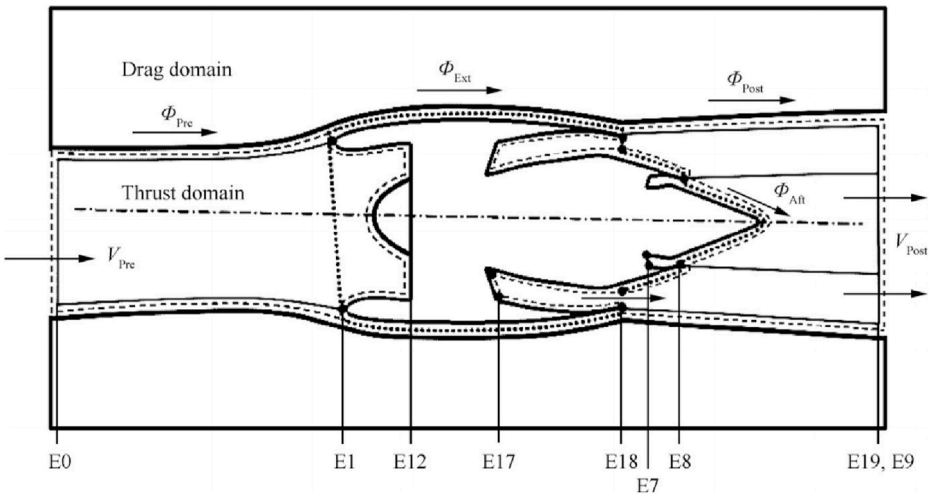

Fig. 11. Control volumes for TDB of powered nacelle. From Ref. [65].

Table 7
Force definitions for TDB [63,83].

Quantity	Definition
Gross thrust	$F_G = F_{G9} + F_{G19}$
Standard net thrust	$F_N = F_{G9} + F_{G19} - F_{G0}$
Overall net thrust	$F'_N = F_{G00} - F_{G0}$
Ram drag	F_{G0}
Pre-entry force	φ_{pre}
Post-exit force	φ_{post}
Nacelle cowl drag	φ_{nac}
Core cowl drag	θ_{cc}
Afterbody plug drag	θ_{plug}
Pylon scrubbing drag	θ_{pylon}
Modified gross thrust	$F''_G = F_G + \theta_{plug} + \theta_{cc} + \theta_{pylon}$

3.1.2. Entropy-based wake-plane methods

Oswatitsch [91] first adopted an entropy equation to deduce the profile drag in steady compressible flow. The survey plane for entropy changes in the wake is also required to position far downstream from the body. Giles [92] proposed to relate velocity deficits to stagnation enthalpy and entropy in the Trefftz plane. The profile drag is then derived. van der Vooren [93] derived velocity deficits in connection with irreversible effects, such as viscous losses and shock waves, and reversible isentropic vortices. Kusunose [94] developed a far-field method for power-on configurations, for which powered propulsion systems are installed onto aircraft, based on a small perturbation theory.

3.1.3. Entropy-based phenomenologicals methods

Paparone [95] put forward to formulate the streamwise velocity as a function of perturbations of entropy, total enthalpy and pressure. By expanding the formulation into Taylor series, different drag contributors are identified. The high order terms are neglected, while the second order reserved to extract the viscous drag. The formulation breakdowns the drag into the viscous, wave, and induced drag components. In a numerical simulation, apart from the entropy that is physically generated inside the viscous and shockwave zones, artificial entropy exists throughout the whole computational domain due to numerical dissipations. The artificial entropy also leads to drag on the body and is included in the near-field/far-field balance. The spurious drag can be obtained by integrating irreversible velocity deficits within a volume which is outside the viscous and the shockwave volumes, which are identified in reference to numerical sensors, reviewed in Ref. [96]. In addition to the mesh quality, studies have been performed to analyse other spurious drag contributors such as boundary conditions, domain size, and subcritical and transonic flow regimes [97,98]. The method proposed in Ref. [95] was utilized to extract the drag for the NASA common research model (CRM) [99]. Tognaccini [100] extended this method to extract the thrust for powered configurations in addition to the drag. Destarac [86] proposed a concept of irreversible streamwise velocity for the viscous and drag integrals, as well as the spurious drag integral. The method has been exanimated in many applications, for example, the NASA CRM wing body with a horizonal tail [101].

Local phenomenological far-field methods are featured of 1) decomposing drag components in terms of physical flow phenomena; 2) discerning drag sources; and 3) eliminating the spurious drag by means of tailored control volumes for the drag integrals. In addition, mesh quality is examined in terms of the spurious drag. Vos [102] showed reduced grid sensitivity and 20 dc differences for NASA CRM of DPW-IV for far-field methods, compared to the near-field. The same case was studied in Ref. [103,104] with similar conclusions. Deng [105] confirmed the better drag result for CRM using far/middle-field. As a drawback, a number of manual adjustments to tune the sensors determining the volumes interested by viscous, shock and artificial dissipation losses are required. The cut-off parameters of the sensors that are set

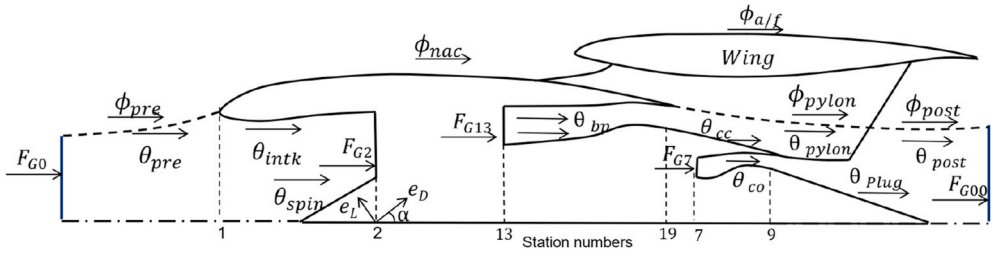

Fig. 12. Installed powered nacelle force decomposition for TDB. From Refs. [84].

to identify viscous and wave drag sources have been empirically determined. As reported in the literature, the parameters are general for various mesh quality and numerical methods. Nonetheless, identified source regions are extended with a margin of several layers of mesh cells. Due to the volume integrations over a large number of mesh cells, the computational time and memory costs of them are larger than other drag bookkeeping methods. Furthermore, to date there are no criteria that explicitly set up sensors for the induced drag sources, although the sensors for the viscous and wave drag have been clearly described with equations and validated with CFD simulations.

3.1.4. Exergy-based phenomenologicals methods

A far-field method based on the thermodynamics first and second laws was proposed by Arntz [106]. Energy is decomposed into exergy and anergy [107]. The exergy can be converted to work, while the anergy is irreversible and useless. Thisexergy-based method by Arntz was applied to analyse the aerodynamic performance of powered civil aircraft configurations, for which the flow was simulated using RANS equations. One of the configurations is a boundary layer ingesting (BLI) propulsion system for a blended wing-body aircraft. In Arntz's method the shockwave region is required to identify within a control volume. This cannot be realized in WT tests. In recent studies [108,109], the problem was tackled by replacing the volume integral with a surface integral over a downstream survey plan using Kusunose's drag bookkeeping method [94,110]. It was found that the survey plane is ideally placed more than one chord lengths downstream of the body, but this distance must be less than 3 or 4 chord lengths.

3.1.5. Vortex-force methods (Lamb-vector method)

The connections between vortex forces, lift and drag, were derived for incompressible flows by Wu [111]. The vortex forces are related to the Lamb vector $\mathbf{I} = \boldsymbol{\omega} \times \mathbf{u}$, with $\boldsymbol{\omega} = \nabla \times \mathbf{u}$ the vorticity. Since the unsteady Navier-Stokes equations are used in the derivation, the method is generally applicable to the force breakdown for both steady and unsteady flows past either stationary or moving/deformable bodies. In the study by Marongiu [112], this method was extended to decompose time-averaged forces in high-Reynolds number flows based on steady flow statistics, which were obtained using RANS CFD simulations. Moreover, this study addressed the connection between the vortex force and the induced drag.

Wu's method is only valid for incompressible flow. This limit was resolved with compressible correction by Mele [113]. The force volume integrals in the vortex methods adopt an arbitrary control volume, where the vorticity is not negligible. For the surface integral of the profile drag in this method, the far-field boundaries of the control volume are utilized. This strategy for setting up the control volume of the vortex methods is different from those of the wake-plane and phenomenological methods. The wake-plane methods employ a far-field downstream survey plane. The plane is restricted to coincide with the Trefftz plane, or with a moderate limit that the flow between the plane and the Trefftz plane. The phenomenological methods utilize local viscosity sensors to identify the control volumes.

3.2. Computational modelling of integrated engines

The assessment of installation effect can be carried out by comparing the force obtained by superimposition of individually operating components with the force acting on the overall assembly, which is split into wing body (WB), Pylon (P), and Nacelle (N):

- Installation effect = [Wing Body Nacelle Pylon] - [Wing Body]

The traditional workflow for engine integration relies on the design of aircraft components based on isolated analysis and successive assembling to evaluate interference effects [114]. In that phase, changes to the orientation and positioning of nacelle with respect to wing, as well as partial redesigning of the interfaces, are used to mitigate the interference and comply with other constraints, defining an interference boundary where the nacelle should fit. This is set by safety and maintenance criteria, such as ground clearance, nose-gear collapse, engine failure.

In the past, due to the inadequacy of numerical tools, the quantification of engine installation penalties was assessed primarily in wind tunnel tests [8,115,116]. This will be examined more in detail in the next section. Here, the main numerical tools developed over the years are reviewed. Important projects tackling the effect on UHBPR on installation performance were conducted within European initiative led by DLR and ONERA starting from the 90's in the projects DUPRIN-I, DUPRIN-II, ENIFAIR and AIRDATA [6,9,116–120], where computational simulations of increasing fidelity were performed parallel to wind tunnel tests. Rossow [117] compared results from experiments and Euler calculation for DLR-F6 wing model installation effects. The installation drag at $M = 0.75$ and $C_L = 0.5$ was measured in 42 drag counts (1 dc = 0.0001), amounting to 14% of the total. A detailed description of the flow field variation due to the throughflow nacelle is provided. Despite the inability of the inviscid computation to correctly replicate the pressure distribution and in particular the shock wave position, in the pylon/wing junction and nacelle cowl good agreement was observed. Inboard of the pylon, the close nacelle mounting and the streamline curvature induced by wing sweep create a region of local acceleration in a narrow gulley formed by wing, nacelle and pylon, where supercritical conditions are formed and terminated by a shock wave in the wing lower side. Near the rear of the pylon, the pressure recovery on the wing lower side can induce adverse pressure gradients promoting separation. On the wing upper side, the nacelle reduces the local incidence, causing a forward shift of shock wave position over the whole span. Extension of the study using a viscous solver with Spalart-Allmaras turbulence model and unstructured grid up to 8.5 M nodes is reported in Brodersen [121], where the same wing body was tested with different nacelles, including one for a VHBPR engine. Compared to experimental data, the total drag found in simulations showed an offset of approximately 16 dc, but at reference lift the differences due to nacelle position could be measured within 2 dc accuracy. The installation drag was consistent with wind tunnel values and for a conventional CFM-56 long nacelle amounted up to 30 dc. A slight overprediction of flow acceleration near wing nose and on the lower side close to the pylon inboard side was found in numerical simulations. This effect was systematic for all cases but did not deteriorate installation drag prediction and the outcome of the engine positioning study. Within the same EU programme, Rudnik [9] compared installation effect for three engines of BPR 6, 9.2 and 15.7, using a Euler code plus 3D viscous boundary layer corrections on the DLR ALVAST wing body, resembling an Airbus A320. The UHBPR caused the largest upstream shock movement on wing upper side due to reduced local incidence and lower side acceleration for the jet passing close to the wing. In addition, it also exhibited a higher spanwise lift loss, compared to lower bypass engines.

Another valuable experimental and numerical database for aircraft and installation modelling comes from the large experience from a series of AIAA Drag Prediction Workshops (DPW) [122], began in 2001. The success of the initiative led to the design of a modern aircraft body for long haul applications, named NASA Common Research Model (CRM) [123,124], that has been chosen as reference geometry starting from the fourth workshop and used in several CFD and experimental studies at different flow regimes [99,125–132], becoming the current baseline geometry in most UHBPR studies. The second DPW first addressed the integration effect for DLR-F6 wing body with axisymmetric long throughflow nacelles similar to CFM-56, used in the aforementioned EU programmes of '90s. The aircraft model was known to have pockets of flow separation at wing root and wing/pylon junction, for which it was difficult to draw meaningful conclusions on drag increment and establish systematic grid convergence. Experimental tests at DLR and ONERA recorded an increase of 43 drag counts at $M = 0.75$ and $C_L = 0.5$, whilst

RANS numerical simulation from the same research centre estimated a variation from 41 to 48, depending on the grid level [133]. Drag breakdown also indicated a higher sensitivity of inviscid drag to angle of attack, but a low sensitivity of the same component to installation.

After changing to CRM geometry, a more systematic a uniform approach could be adopted for data comparison and grid convergence [134], providing precise gridding guidelines and topologies. A review of the results for all the DPWs is given by Tinoco in Ref. [135], reporting issues and inconsistencies across the participants and giving recommendations for future elaborations. In DPW-VI, the differences in WB drag from a medium to an extrapolated infinite resolution grid was in the order of three-four drag counts. The author, however, points out how direct verification of the absolute drag value is not achievable, and rather differenced should be accurately computed. Fortunately, the average drag increment from WB to WBNP converged to the experimental value of 22.8 ± 1.2 dc. As engine diameters are expected to increase in pursuit of improved propulsive efficiency, the engine installation becomes an increasingly important concern. Therefore, the knowledge of the installation effects at the preliminary design stage is crucial for facilitating timely and informed decisions on the design of the engine cycle, nacelle, and airframe integration. A key element in the development of future civil aircraft is robust assessment of the mutual interactions and, furthermore, the thrust and drag characteristics of the combined engine and aircraft configuration. The experiences from the DPWs are useful to develop computational tools and to assess the nacelle installation interference drag for a typical civil transport configuration.

In that respect, numerical results obtained at ONERA using the proprietary finite volume code elsA with Spalart-Allmaras turbulence model for the DPW-VI are presented by Hue [136]. The farfield drag extraction method employed by the authors allows to distinguish between several physical drag components, helping to delineate the principal flow mechanism altering isolated components performance during coupled operation. At $C_L = 0.5$, the total drag coefficient reported was 138.5 dc, in close agreement with experimental data from the same institution [101], where model displacements were recorded and considered during CFD analysis in DPW6, as it is mainly the twist variation responsible for drag increment between stiff and deformed versions, because of variation of span load, pressure field and shock position. At outboard wing section, however, the comparison between CFD and wind tunnel was worse, with overprediction of aft loading found in experiments. In addition, this data appeared dependent on turbulence model formulation, linear Boussinesq hypothesis versus Quadratic Constitutive Relation (QCR) [137] for turbulent stresses. Analysis of drag breakdown from Wing Body (WB) to Wing Body Nacelle Pylon (WBNP) configurations showed that the overall increase found was 21.8 dc. Of this increment, almost 17 dc come from the friction drag, due to increased wetted surface when the pylon and throughflow nacelle are installed under the wing. The remaining 5 dc are due to viscous pressure drag, defined as the part of the viscous drag that is not due to the friction, caused for instance by displacement or flow separation. A closer local inspection reveals that the spanwise lift distribution has locally changed near the engine station, but in a way that the sum is almost untouched. In particular, the shock wave position in the inboard side is mostly affected, with an anticipation of 10–15% of chord at 28.3% of span. Fig. 13 illustrates the spanwise distribution of drag components, making evident that apart from local increase of friction drag near the engine, two bumps are produced in the inboard side for the viscous pressure drag, amounting to +5 dc. Minor separation is also present at pylon trailing edge, while a side-of-body (SOB) separation at wing-fuselage junction is predicted by standard turbulence models, but not found in experiments. The extent of this separation bubble was also sensitive to the turbulent stress formulation and must be reviewed in future elaborations.

For the powered-off nacelle, therefore, the major effect related to drag increase, excluding the higher friction on the larger wetted surface, is the modification of the flow path resulting in shock wave

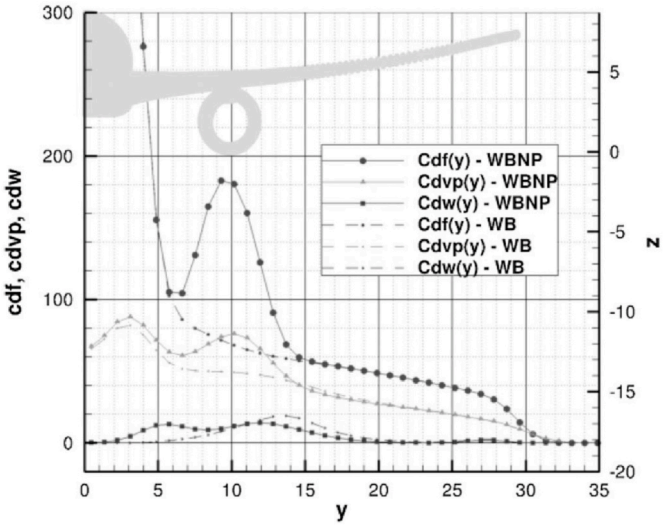

Fig. 13. Friction (CD_f), viscous pressure (CD_{vp}) and wave (CD_w) drag spanwise distribution for WB and WBNP for NASA CRM at $M = 0.85$, Re $= 5 \times 10^6$. From [136].

displacement, boundary layer thickening and consequent variation of the pressure field on the wing. In the powered-on condition, instead, there are two main effects to be considered: the change in drag caused by modification of the flow field around wing and nacelle and the change of thrust caused by variation in velocity and discharge coefficient of the nozzles. These two effects are usually studied separately. It must be recognised, however, that this is not completely physical, since any change in the engine operating point is reflected by a change in the streamtube ingested by the intake, causing spillage drag to appear and thrust variation. For the limitations of current computational approaches and in standard practice, nonetheless, the intake and the exhaust are designed by different specialists and as such their analysis is uncoupled. Zhaoguang [138] reported equations to specify boundary conditions at fan face, based on isentropic expansion from freestream to highlight, and nozzle plane, based on engine total pressure and temperature ratio, when these two boundaries are imposed separately. He also studied the jet interference on DLR-F6 wing at different power setting. At cruise, the main change is a flow acceleration and pressure reduction on the wing lower side, close to the engine axis, causing a global reduction of 0.013 in C_l and increase by 0.005 of C_m. The major differences occurred in the high-lift configuration at take-off power, with the lift slope increased and the pylon outboard region pressure distribution most affected. Zhang [65] performed viscous calculation of powered nacelle for a twin regional aircraft at cruise Mach number of 0.785, ensuring mass flow continuity between fan face and nozzle planes. Compared to an equivalent throughflow nacelle, a simultaneous lift loss and drag rise could be noted. The uncertainty on thrust loss due to nozzle velocity coefficient was estimated to be 2 dc, whilst the pylon drag was 4.9 dc. The jet interference with the wing lower side caused the appearance of increased suction, close to the engine axis. A region of local flow acceleration is visible in Fig. 14, comparing the throughflow with the powered case.

3.3. Nacelle position and optimisation studies

An important topic on engine integration is the optimal positioning of the wing-mounted nacelle, which has been addressed by several authors, assessing the sensitivity to drag and thrust with nacelle location. An interesting source describing the workflow, the activities and the methods for propulsion integration on Boeing 777 is the conference paper of Berry [139]. The author enumerated a number of aerodynamic and non-aerodynamic requirements driving the powerplant installation.

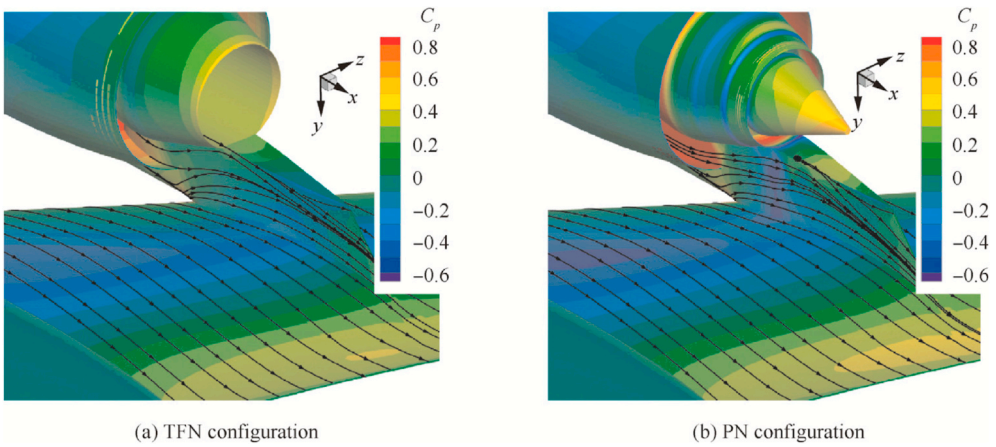

Fig. 14. C_P distribution for throughflow and powered nacelle for a twin-engine regional jet, at $Ma = 0.75$, $Re = 2.4 \times 10^7$, $C_L = 0.55$. From Refs. [65].

Among the first, the nacelle size and position affect wing shape, drag figures, local wing circulation, wing span loading and structure, strut contours and weight, vertical tail size, and noise emission. Non-aerodynamic criteria are related to ground operation and safety. The maximum engine size is limited also by ground, runaway, taxing and airport gate clearances. Sufficient roll clearance must be kept for crosswind landing and flat tires, while vertical ground clearance must be enough to avoid engine scraping in the event of nose gear collapse. The spanwise location must also consider passenger door escape slide, loading ramps, suction and blowing zones, turbine disk bursting zones, nose gear water spray cone. Fore/aft nacelle position influences wing aeroelastic response and structural elements sizing. Vertical position must cope with jet interference on the wing, the trailing edge deployed flaps and the horizontal tail plane. The actual bounding zone for nacelle installation is, therefore, limited by a series of constraints that can be introduced in the form of lateral bounds to the design variables for engine positioning analysis.

Experimental and computational studies on the influence of engine position on installation drag were performed during the aforementioned EU initiatives of the '90s, including VHBPR and UHBPR models. Rossow [118] reported an inviscid study of variation of nacelle location for a BPR = 11 and BPR = 23 engine on DLR-ALVAST body. The different dimensions of the models led to different choice of mounting distance, which is given throughout all this paper as from Fig. 15, computed from wing leading edge to nacelle trailing edge and with horizontal displacement positive in the downstream direction. For the VHBPR, reducing the horizontal distance from the wing resulted in a progressive upstream shift of the upper surface shock wave and reduction of flow acceleration on wing lower surface. These two effects compensate each other, such that the global lift was little affected. Overlapping of nacelle and wing (a positive x/c value) further reduced the effect on the upper wing, whereas the lower surface showed an enhanced interference, with a flow acceleration in the first 15% of chord, inboard of the pylon. The same behaviour on the lower side was continuously seen when the UHBPR was horizontally moved towards the wing leading edge. The wing suction side remaining unaffected, the flow acceleration on the lower surface and the adverse pressure gradient were not compensated, with the lift always penalised. The sensitivity of vertical position, instead, resulted much lower, possibly realising a closer coupling with the wing helping to respect ground clearance. These findings are confirmed in Ref. [9], although it is concluded that due to the influence of the exact nacelle shape and geometric factors, a general rule cannot be drawn. Nonetheless, the indication is that a forward movement can alleviate interference and vertical gap is of limited importance. Experiments and RANS verification for the same wing body using VHBPR turbofan highlighted a reduction of 2 dc in installation drag by aligning the nacelle trailing edge with the wing leading edge and a larger sensitivity at low C_l [121].

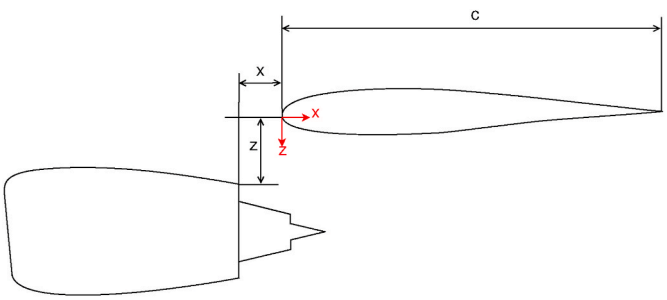

Fig. 15. Underwing nacelle positioning.

Oliveira [114] presented results of integration study for Embraer 170 aircraft using 3D Euler solutions, deemed to be conservative in terms of pressure coefficient alteration caused by engine assembly. The jet interference on the lower wing surface were remarkable, causing two suction peaks at about 30% and 60% of chord, respectively, close to the pylon. The upstream movement of the engine had an opposite impact on the peaks, alleviating the first one but slightly increasing the second. This set an optimum value to minimise both of them, which are, instead, less sensitive to the vertical distance from the wing. Due to the change in wing circulation and nacelle upwash, in addition, a small toe angle is also necessary to align the relative flow to the highlight plane at cruise.

Sibilli [140] reported the implementation of a propulsion system integration (PSI) module, applied to two new engine concepts from NEWAC EU project, a three-shaft direct-drive high bypass ratio turbofan with an intercooled core, and a two-shaft geared high bypass turbofan with actively controlled core. The numerical tool was devoted to quantification of net propulsive force influence of engine positioning. Nacelle and exhaust were designed according to engine specifications for size, BPR, mass flow rate, thrust and total status at nozzles. Nacelle was designed according to NACA standard procedures, while exhaust system considered geometric constraints and was manually refined through successive RANS CFD simulations. The nacelle generated were finally installed on NASA CRM, after a manual improvement of pylon design to eliminate shocks on its inboard side. The half aircraft model was simulated using steady RANS, with the $\kappa - \omega$ turbulence model and 14 M nodes grids. The installation effect was then evaluated at different vertical and horizontal displacement of the nacelle. Confirming the indications from previous studies, the horizontal position had the largest effect on interference drag, which was alleviated by enlarging the upstream gap with the wing. By using an engine performance modeller, the impact of engine distance on cruise fuel consumption was estimated to be 3.67% between the extrema for the intercooled engine, and 6.4% for

the actively controlled core engine.

Christie [21] studied the interference effect of nacelle position with respect to wing using CFD and proposed a modified near-field method to compute nacelle drag. A test matrix was derived to assess the installation effect on NASA CRM of two nacelles, one with diameter 3.133 m and the other with diameter 4.018 m, tested for three flight conditions and three positions, for a total of 18 cases. Simulations were carried out using a commercial solver with steady RANS and a 30 M node grid. A large variation in nacelle drag and a different trend was found for the two configurations at different flight conditions. The installation drag resulted to be negative in most of the cases, with only two positions where a large increase of airframe drag was caused by wing shock pattern alteration. This also led to change of pressure distribution and loss of lift. The author remarked that, for this reason, comparison should be done at equal lift coefficient, rather than equal angle of attack, as in practice the lift should be recovered by increasing the incidence and, in turns, the drag. In addition, using a propulsive system integration module developed to analyse mission fuel burn including installation effect, he found that the interference has a greater impact on fuel burn for larger engines.

Stankowski [141,142] presented a computational framework for the assessment of engine installation effects, by analysing nacelle position and size and phase of flight. The first paper is devoted to the validation of the computational method for the drag prediction of the NASA CRM, while the second is focused on the effects of nacelle position. Two engines with different BPR were installed on NASA CRM. The first engine, denoted E1, was representative of a typical modern turbofan, with BRP = 10.4 and overall pressure ratio (OPR) of 50. The second, denoted as E2, had a BPR = 17.8 and OPR = 58 and featured a diameter 1.23 times larger than E1. According to engine performance and thrust requirement of 55686 N at M = 0.82 and 35000 ft of altitude for CRM, four flight phases were defined, in terms of engine operating conditions. The CFD tool was first validated for axisymmetric throughflow nacelle and then applied to NASA CRM. The simulations employed a commercial density-based solver, with the $\kappa - \omega$ *SST* turbulence model and 30 M nodes fine grid for WBNP configuration. The difference of computed drag at $M = 0.83$ and $C_l = 0.5$ between CFD and experiment was 8.4 dc for the fine mesh, whilst the installation drag was within 1 dc. The effect of engine position was evaluated on a nine points matrix, using force decomposition to highlight the different contributions to the drag and thrust. As expected, the interference on net thrust was mainly affected by the horizontal location. For E1, in all the positions the nacelle drag was reduced, from 2.6% to 5.1% of E1 standard net thrust at cruise. This gain was offset by increase of airframe drag at larger upstream distance. The trend indicated a detrimental effect where axial location was increased with simultaneous reduction of vertical distance. For E2, the net propulsive force variation across the test matrix was 1.3% of reference net thrust, compared to 1.7% of E1. Again, the nacelle drag improved in all the positions, with greater alleviation for upstream displacement, but worsening of airframe drag. The sensitivity to installation position was, overall, less than E1. Comparing the effect of engine size for the same nacelle trailing edge location, relative to wing leading edge, a noticeable modification of the flow field was observed, visible in the Mach number contours of Fig. 16. In particular, engine installation caused an upstream upper surface shock wave shift and appearance of a two shock pattern outboard of the pylon, with a more pronounced variation for E2. The mitigation of the suction peak brought a loss of lift in both the cases, followed by a decrease of lift-induced drag. On the lower side, due to the lower pressure ratio of bypass nozzle for E2, modest jet interference was observed. Overall, the installation effect was 33 dc and 45 dc for E1 and E2, respectively, with corresponding variation of 5 dc and 3 dc between the different positions. These data are in broad agreement with those previously found in experimental campaigns, although for engine with relative lower diameter. For the specific case, E2 featured a beneficial positive thrust contribution on the exhaust surfaces offsetting the augmented nacelle drag, and a reduced interference sensitivity. The result, however, appears dependent on the engine thrust condition and the cowl design, and a generalisation might be incautious, although the large engine can be considered representative of a future UHBPR. In terms of fuel consumption over a nominal cycle, the E2 benefited from a −4.8%, compared to E1, when the effects of engine weight, installation, and throttle dependent interference were included.

Within the same research group, and following the work of Stankowski, Otter [143] continued the analysis on exhaust installation effect, using the same engines E1 and E2. The author analysed the sensitivity of velocity coefficient C_V and discharge coefficient C_{disch} to engine installation position, again on a nine point matrix over a similar range, and aircraft angle of attack. Example of pressure coefficient distribution at different incidence is shown in Fig. 17. The largest engine exhibited a greater sensitivity of C_V to axial position, up to three times bigger than E1. It was explained by a modification of the core cowl and core plug afterbody forces and the lower specific thrust. The change in ambient pressure where the nozzle discharges caused, instead, a variation of core C_{disch}, from −2% to −10% for E1 and from 0.75% to −1% for E2. This has an importance in engine operating conditions, as either it will not be able to operate at the prescribed uninstalled point, or a modification of nozzle area will be necessary to reset the operative point. The bypass nozzle, which was choked, exhibited only a very limited sensitivity. In addition, over a range of incidence from 0° to 4°, the core discharge coefficient C_{disch} varied from 3.7% to −13%. For E1, this variation was not monotonic with the angle of attack in certain positions, whilst in general E2 had a decreasing trend. The velocity coefficient was found to have a more uniform increasing variation, instead,

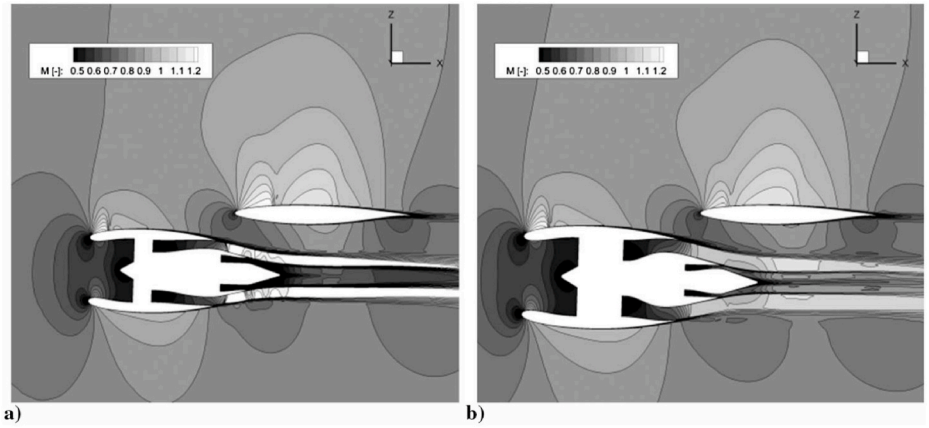

Fig. 16. Mach number contours for E1 (a) and E2 (b) engines at cruise. From Ref. [142].

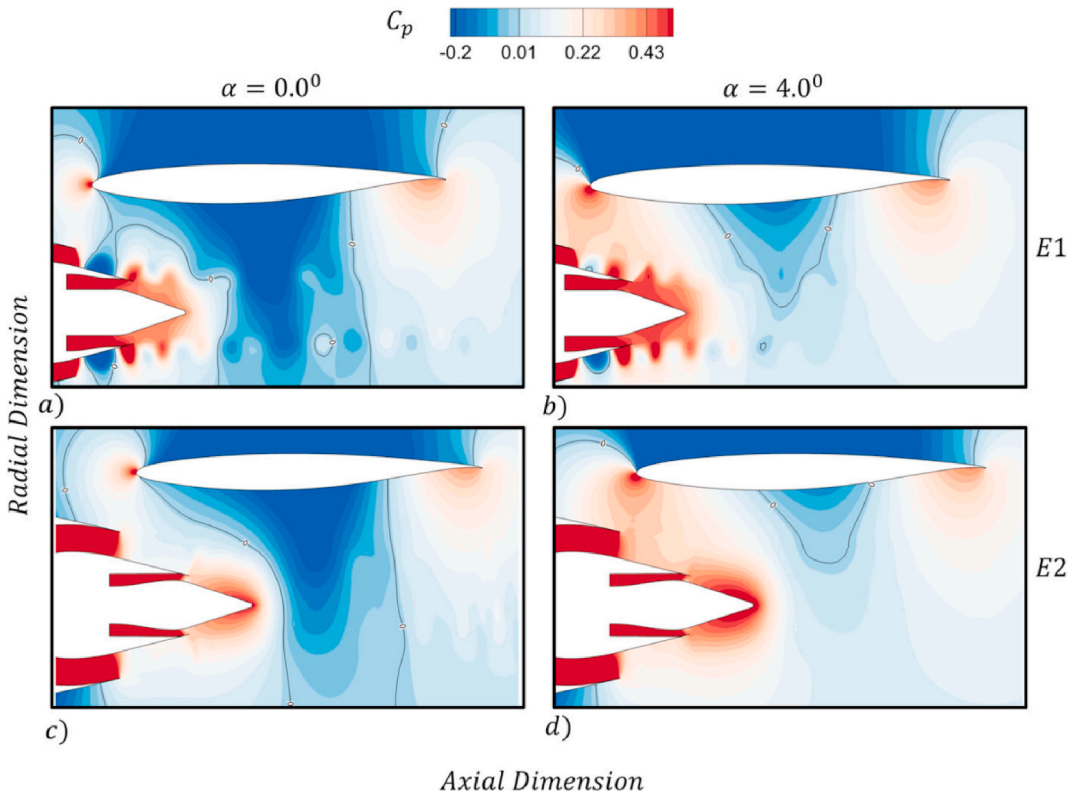

Fig. 17. Pressure coefficient at discharge zone for E1 (upper) and E2 (lower) engine at different incidence. From Ref. [143].

starting from negative values at zero incidence and becoming positive at largest angle. This sensitivity highlights the necessity of considering installation and flight conditions for the design of the exhaust system, as thrust changes need to be compensated by varying the engine power or aircraft attitude.

Ritter [144] studied a go-around case, where landing is aborted and the aircraft tries to rapidly recover thrust and altitude, using an infinite swept DLR-F15 wing section with high-lift devices and a 2.9 m diameter engine of BPR = 19, whose position was varied. The sensitivity analysis involved ten positions, with 50 mm steps in vertical and horizontal displacement and $\alpha = 0^\circ, 5^\circ, 10^\circ$. An in-house CFD solver with Spalart-Allmaras turbulence model and a hybrid unstructured grid of 76 M points were used. Moving the engine from the reference condition, a complex pattern for lift and drag change was recorded, without a general trend. Every fore/aft displacement led to a loss of lift, which was even higher for negative vertical movements. This vertical offset determines the level of interference between the jet and the high-lift devices, assuming in this case a more relevant importance, compared to the sole drag figures at cruise. The lift-to-drag ratio generally improved for wider coupling.

The first attempts of automatic optimisation of nacelle shape and position were made with the use of Euler solvers. Koc [145] optimised the inboard wing shape, wing/pylon junction and nacelle vertical position and pitch angle for the DLR-F6 wing body. The unstructured grid had 2.5 M cells and Hicks-Henne's functions were used in conjunction to an adjoint solver and Sequential Quadratic Programming (SQP) optimisation algorithm. As the baseline was characterised by a strong shock wave in the inboard pylon side at climb, where $\alpha = -2.9^\circ$ and $M = 0.74$, the inviscid optimisation allowed to suppress the loss and gain 19.7% of drag or 16 dc, at fixed C_L.

Smith [146] reported a similar result, that is the elimination of shock wave in nacelle lower lip and trench region after inviscid optimisation of a throughflow nacelle and wing shape, with also substantial improvement of the upper wing shock pattern. The baseline geometry represented a single-aisle transport with a 34.38 m of span, an aspect ratio of 10.0 and cruise Mach number of 0.785. The engine featured a fan diameter of 2.1844 m and a BPR of 15 and it was placed with a vertical offset of 13.4% of local wing chord at nozzle lip from wing leading edge. The nacelle shape, pitch a toe-in angles were varied throughout the optimisation, in addition to the pylon shape. The final inviscid design was corrected for viscous effects and a wind tunnel model with a representative turbo powered simulator (TPS) was built and tested. Pressure Sensitive Paint (PSP) measurement highlighted good agreement with computational data, as shown in Fig. 18, confirming that relevant interference phenomena are related to inviscid effects and pressure forces must be monitored when studying, testing or optimising WBNP configurations. Jing [147] used free-form deformation (FFD) and particle swarm (PSO) for the optimisation of a throughflow nacelle vertical and horizontal position on DLR-F6 wing body at constant lift. The nacelle shape was kept unchanged and the pylon smoothly modified to account for each new position. The optimisation was conducted at cruise, $M = 0.75$, using a RANS solver with $\kappa - \omega$ *SST* turbulence model and a multi-block structured grid. The optimal design for minimum drag coefficient exhibited a reduced flow acceleration in the inboard side of the pylon, a reduction of suction peak and a dimmed interference with the wing, leading to a 3.6 dc improvement.

Epstein [148] set up an automatic optimisation environment for a multi-point optimisation of a long-haul aircraft with installed nacelle. The kink and tip section of the wing, previously designed stand-alone for minimum drag, were varied to minimise the installation drag. The wing-mounted throughflow nacelle geometry was kept unchanged, positioned close to the wing leading edge, at around 7% of local chord, and not overlapped with it. Three points were considered for the application of the genetic algorithm (GA): two at cruise, $M = 0.845$, $C_L = 0.575$ and $M = 0.86$, $C_L = 0.575$, and one at take-off, $M = 0.20$. A pair of single point optimisation at cruise first achieved a drag reduction of 36.3 and 24.5 dc, respectively. This occurred by changing the wing

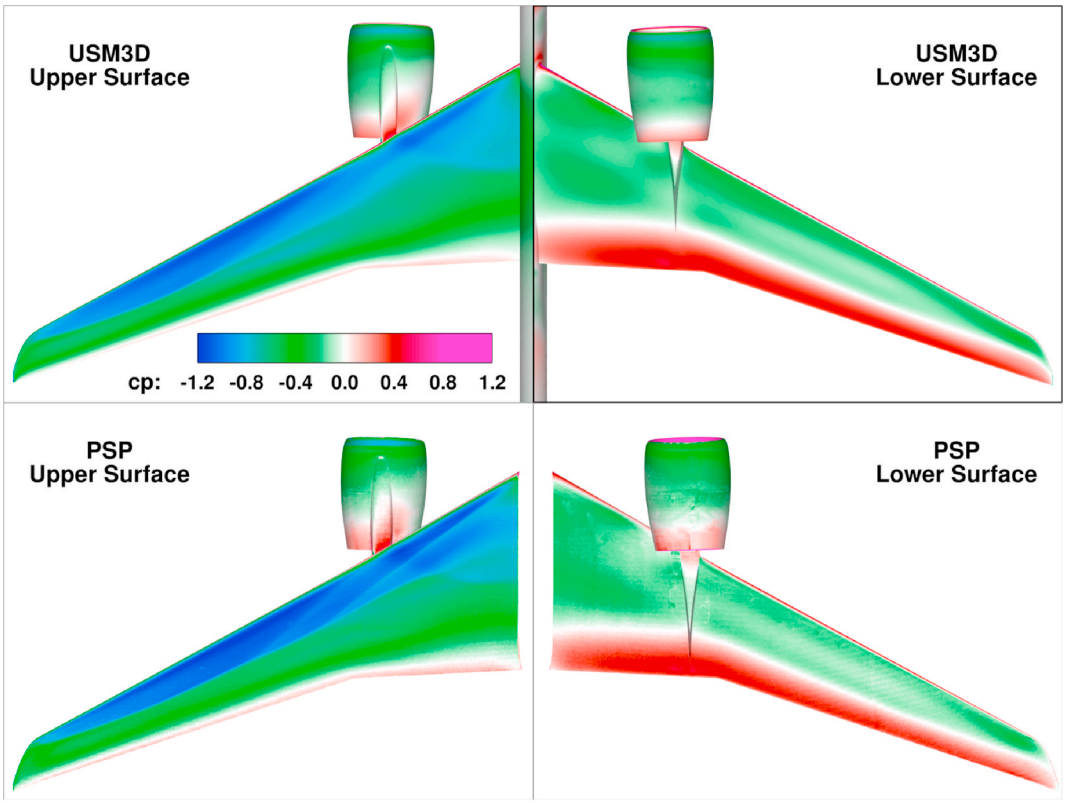

Fig. 18. Comparison of pressure field from numerical simulation and wind tunnel PSP for optimised wing/nacelle. From Ref. [146].

sections only, without varying the distance from wing leading edge to the nacelle and thus the gulley height. A second weighted multi-point run, considering also the take-off, changed this result to 33.9 and 28.6 dc. Analysis of the flow field showed that it was obtained by a more favourable upper side shock wave pattern and improvement especially closer to the trailing edge, where a second shock originally took place. The attenuation of the interference drag was evident even from the restored convexity of the drag polar over a wide range of lift coefficient.

Lei [149] recently employed SQP optimisation algorithm and FFD for wing shape parameterisation at eleven spanwise stations, allowing also small changes on nacelle vertical, horizontal and toe-in position. An adjoint RANS flow solver based on Spalart-Allmaras turbulence model on a 16.8 M multiblock structured grid was employed on the NASA CRM at cruise. The under-wing mounted engine had a BPR of 8 and suitable boundary conditions were applied at fan face, bypass and core nozzle to simulate a powered flight. The optimised aircraft achieved a constant-lift global drag reduction of 11.4 dc, 9.1 of which coming from the engine and 4.0 from the wing. By closer inspection of the flow field, the upper wing shock wave appeared to have been largely smoothed by the optimiser. The negative jet interference on the wing lower surface was attenuated by a forward movement on the nacelle, which, combined with an increased wing camber, led to suppression of suction and reduction of the flow velocity in the nacelle-wing-pylon channel.

Hooker [150] presented a thorough revision of an alternative over the wing nacelle (OWN) installation, as compared to traditional under-the-wing (UWN). Four engines with different bypass were considered: a separate-stream (SSTF) and mixed-stream (MSTF) turbofan with BPR = 5.5, a very high BPR of 9.0 and an ultra-high BPR of 38.0. CFD simulations were carried out on a 12 M unstructured mesh and a NASA RANS flow solver. Each concept was representative of a different technology level, from typical low bypass to ultra fan, and was tested over 70 positions, including OWN LE, OWN TE and UWN mounting. Considering first the case of the SSTF, for OWN at cruise Mach of 0.85 the interference effect appeared severe, whilst for UWN a farther placement gave a lower or even negative interference, compared to the clean wing. This trend appeared the same for all engine sizes, with a notable diminished effect for MSTF. Overall, the key finding of the investigation was that for OWN TE the total interference drag was large, but the nacelle component, the difference between installed and isolated nacelle drag, was remarkably low, opening to possible optimisation of nacelle/pylon to reduce airframe drag. On the contrary, OWN LE had reduced wing drag, caused by an extended leading edge suction region producing a forward force. Based on these findings and a preliminary exploration, six pre-optimised configurations were selected for a second optimisation, including the pylon. The OWN TE UHBPR finally achieved a ML/D ratio of 16.7 at cruise, compared with 16.0 of UWN UHBPR, with also a 6.3% estimated reduction in EPNL noise, at the cost of a weight increase of about 1.4%. The study interestingly shows that, despite the greater difficulty for the design and the enhanced mutual effect of engine and wing flow field, by shape optimisation of WBNP it might be possible to reach over-wing solutions competing with traditional under-wing mounting. More recently, Savoni [151] presented an OWN installation study for a 100PAX aircraft, confirming the need to consider nacelle, pylon and airframe shape modification for this configuration, given the large effect on the flow field brought about by engine integration, causing strong wing shock with induced separation on nacelle cowl and pylon.

The summary of the studies presented is reported in Table 8. For each author, it is indicated the year of publication, the activity performed (shape optimisation or study of selected engine positions in a test matrix (TM)), the type of nacelle (TF = throughflow, PN = powered nacelle via boundary conditions) and, when available, the equivalent bypass ratio, the aircraft body on which the engine was mounted, the turbulence model, the grid size and type (U = Unstructured, MBS = Multi-Block Structured), and the mounting position as from Fig. 15. The table provides a general overview on the evolution of numerical modelling of nacelle placement and shape optimisation of wing body/nacelle/pylon configurations. The first computational studies made use of inviscid

Table 8
Summary of studies on nacelle position or optimisation for high bypass engines.

Author, year	Activity	Nacelle	BPR	Aircraft Body	Turb. Mod.	Grid Size - Type	x/c	z/c
Rossow, 1994 [118]	Eng. Pos. on TM	TF	23	DLR-ALVAST	Euler	0.65 M U	$-0.41 \div -0.30$	$0.07 \div 0.11$
Rudnik, 2002 [9]	Eng. Pos. on TM	TF	11	DLR-ALVAST	Euler + viscous	0.65 M - U	$-0.052 \div 0.05$	$0.12 \div 0.19$
Brodersen, 2002 [121]	Eng. Pos. on TM	TF	11	DLR-ALVAST	S-A	8.5 M - U	$-0.05 \div 0.0$	0.12
Oliveira, 2003 [114]	Eng. Pos. on TM	PN	5	Embraer 170	Euler	1.0 M - U	$-0.28 \div -0.05$	$0.08 \div 0.16$
Koc, 2005 [145]	Opt. Wing, pylon, nacelle shape and pos.	TF	–	DLR-F6	Euler	2.5 M - U	–	–
Sibilli, 2012 [140]	Eng. Pos. on TM	PN	–	NASA CRM	$\kappa-\omega$ *SST*	14 M - U	-0.25 ± 0.15	–
Smith, 2013 [146]	Opt. wing, pylon, nacelle shape	TF	15	Custom Long Haul	Euler	14.2 M - U	–	0.134
Jing, 2013 [147]	Opt. wing, pylon, nacelle pos.	TF	–	DLR-F6	$\kappa-\omega$ *SST*	–	–	–
Hooker, 2013 [150]	Eng. Pos. on TM + Opt. wing	PN	9–38	Custom Long Haul	RANS	12 M - U	–	–
Epstein, 2016 [148]	Opt. wing	TF	–	Custom Long Haul	RANS	1.3 M - MBS	–	–
Christie, 2016 [21]	Eng. Pos. on TM	PN	11.2	NASA CRM	$\kappa-\omega$ *SST*	30 M - MBS	$-0.074 \div -0.2$	$0.05 \div 0.116$
Stankowski, 2017 [142]	Eng. Pos. on TM	PN	10.4–17.8	NASA CRM	$\kappa-\omega$ *SST*	30 M - MBS	$-0.058 \div -0.39$	$0.056 \div 0.169$
Otter, 2019 [143]	Eng. Pos on TM	PN	10.4–17.8	NASA CRM	$\kappa-\omega$ *SST*	34.6 M - MBS	$-0.05 \div -0.35$	$0.07 \div 0.17$
Lei, 2019 [149]	Opt. wing, nacelle pos.	PN	8	NASA CRM	S-A	17 M - MBS	–	–

solvers with unstructured grids. Although limited in accurately predicting shock wave positions on the wing, which depend also on boundary layer thickness and displacement, and unable to measure friction drag, many authors have shown that the flow phenomena occurring near the engine-wing junction are dominated by inviscid effects and substantial reduction of wave drag can be achieved even with a Euler-based optimisation. On the other hand, as resulting from nowadays standard RANS calculations, pressure forces are about two order of magnitude higher than viscous ones, the latter scaling roughly with nacelle wetted surface. As regards the engine positioning, from a purely aerodynamic point of view, there are two indications coming from the numerical studies. The first one is that the horizontal position has a larger effect on the interference, compared to the vertical distance from the wing. The second, coming mainly from the earlier research, is that a farther upstream movement of the engine is beneficial to reduce the installation penalty. The validity of both theses for UHBPR, however, is questioned by more recent studies, showing that the interaction is such that several degrees of freedom can contribute to the mitigation of the installation drag. Besides there might be a different effect on the thrust, which is more sensitive to the discharge conditions for low specific thrust engines with core nozzle typically unchoked. Neglecting the orientation of the nacelle with respect to the wing, given by pitch and toe-in angles, the vertical and horizontal offset are determined by many other non-aerodynamic considerations, as reported previously. It might be interesting to examine the installation position of under-wing nacelles on existing commercial airplane. Christie [21] carried out a survey of these parameters for different airframe and engine manufacturers. His result is depicted in Fig. 19, where the approximate BPR of each engine has been added. The figure is sparse, but it is possible to recognize some homogeneous clusters. For instance, low bypass engines of '60s and '70s were placed with horizontal overlapping with the wing (positive x/c) and small vertical gap. Airbus aircraft with Rolls-Royce Trent engines of BPR $7.5 \div 9.0$ are roughly located in the range $-0.15 \div 0.0 x/c$ and centred around $z/c \approx -0.11$. On Boeing B777 and B787, the same high bypass Trent engines, however, are vertically closer to the wing, crossing the bounds of the dashed exclusion regions, that was empirically found in early experimental campaigns [115]. Pratt & Whitney geared engines of PW1000 family on Bombardier aircraft, instead, have similar horizontal location but larger z/c offset. In summary, it is not possible to recognize a specific trend for BPR, and rather the airframe manufacturer seems to be better correlated to the installation position.

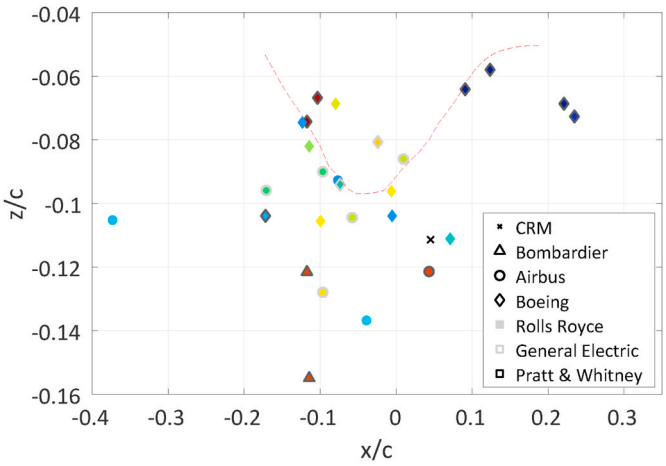

Fig. 19. Survey of nacelle installation position for commercial airplane. Modified from Ref. [21].

Despite the data were found from public available sources and might be not completely accurate, they give the hint that the outcome of the cited aerodynamic studies alone cannot determine a precise region for UHBPR installation. On the contrary, the difficulty in integrating big engines under the wing potentially reduces the aerodynamic design space extent, forcing them to occupy regions that have not been considered before. In addition, the enhanced interference and the new cycle parameters pose greater importance also in the exhaust area, being the net thrust more exposed to in-flight variations related to change of boundary conditions seen by the core and the bypass nozzle, which in turn affect the complete engine power setting and operating point. In this framework, potential improvements might come from the application of automatic optimisation tools coupled to high-fidelity numerical solvers. In the sections describing the advancements on nacelle and exhaust design, it was stressed that complex statistical methods and optimisation algorithms based on CFD kernels have become state-of-the-art tools. Moreover, studies on wing/nacelle/pylon shape optimisation have shown that to a certain extent it is possible to achieve better drag figures when changing the wing shape close to the engine junction and tuning the nacelle position and orientation, thus liberating some degrees

of freedom in an inherently coupled design study. This is particularly true for non-standard aircraft configurations, like over-the-wing mounted nacelles and even more BLI propulsion, where fuselage, wing and intake must be modified at the same time. The level of accuracy that has been reached throughout the years for computational solvers and the availability of a wide variety of optimisation frameworks suggest that a simultaneous wing body/nacelle/pylon coupled design improvement is limited mainly by the high computing time needed and obstacles in full procedure automation, rather than the maturity of the theoretical and numerical tools.

4. Experimental approaches for measurement of engine installation effects

Despite the availability of powerful computational resources and turbulent flow solvers, there exist some simulation scenarios and some models limitations that make a numerical approach unsuitable or unreliable. Eventually, experimental tests still represent an indispensable stage in aerospace engineering. Wind tunnel tests of engine-airframe integration are used, for instance, to assess the installation penalty, the forces acting on the structure and its deformations under powered conditions, the effect of the aerodynamic surfaces and the stability, the off-design behaviour, the ground effects, and the effectiveness of accessory subsystems like thrust reverser. During these experiments, engine simulation is a key factor.

4.1. Similarity

One of the most straightforward methods of simulating an engine is to simply replicate the nacelle geometry, leading to the flow-through nacelle concept. A flow-through nacelle basically only replicates the nacelle geometry and mass flux (capture ratio). The absence of any powered components means that it does not simulate larger than flight speed exhaust jets, shock structures and viscous mixing. An (externally) blown nacelle is used to more accurately represent the exhaust jet, but in turn it cannot replicate the inlet flow field. A powered engine simulator, i.e. a fan stage inside a scaled nacelle, is a more complete approach to simulating both engine inlet and exhaust flow physics. Again there can be various degrees of detail in the simulation of the engine (integration) aerodynamics in the wind tunnel. Similarity with the full scale is maintained by duplicating the geometry and the Reynolds and Mach numbers (a few additional similarity parameters exist but their mismatch and non-constancy is typically neglected). In wind tunnel campaigns with engine integration fousing on the aerodynamic aspects the most important geometric parameters are the external geometry and the exhaust exit areas. The replication of the flow field Mach numbers and mass fluxes requires retaining the fan stage total pressure (and temperature) ratio. In cases of aeroacoustic testing more stringent replication requirements must also be placed on the fan stage and internal duct properties.

The geometric scaling of an engine to wind tunnel size, whilst maintaining similarity parameter values, generally leads to increased rotational speeds and power densities relative to the full scale aircraft. Accommodating the relatively large power requirements in a compact space requires a compact power source. Therefore, traditionally engine simulators have been predominantly powered by compressed air turbines. These are small-scale high-speed turbines with compressed air as the working gas. The compressed air is typically supplied from compressed air plants built nearby the wind tunnel circuit. Hydraulic motors are also known to be used and more recently solid state electronics and electric motors also match the required power densities. Fig. 20 diagrammatically shows a flow-through nacelle, an air-turbine powered simulator (TPS) and a turbofan engine.

While typically the bypass duct flow is simulated well in wind tunnel engine simulation, the full scale engine core-flow is usually replicated to a lesser degree. The air-turbine's main function is to supply the fan stage with power. To accomplish this task the driving turbine consumes relatively a lot more air (from the external source) than its full scale counterpart. The externally supplied cold gas is expanded in the turbine and is subsequently exhausted through a nozzle with a rather low temperature. Turbine design can be such that in some cases the core exhaust Mach numbers could match those of the full scale engine for a certain operating point, but in general they differ to a certain degree. De Wolf [153] discussed TPS technology and similarity using four concept engines with increasing bypass ratio (5, 9, 15 and 26). He also reported the difficulties in maintaining the similarity parameters for core flows of VHBR and UHBR engines in TPS simulation. The requirements led to very stringent if not unrealistic TPS turbine designs. The author presented a number of options to arrive at more realistic turbine designs. It was recommended to maintain the geometric properties of the core and its exhaust in favour of maintaining the core nozzle pressure ratio. This led to unrepresentative high Mach numbers of the core flow, but maintained (approximately) the outer diameter of the jets and the correct pressure distribution on the core cowl. Alternatively the core exhaust exit area can be increased but this is less favourable because the geometry and jet size get modified. Concerning exhaust jet speeds, full scale engines typically have core-to-bypass jet speed ratios slightly over but close to one (extending towards 1.5 for lower bypass ratios). For TPS units this ratio drops closer to 0.7 upon nozzle pressure ratio duplication. In circumventing practical limitations of air-turbines core nozzle pressure ratios may be increased to beyond their full scale counterpart. This would in turn bring the core-to-bypass jet speed ratio closer to one. Therefore in many cases TPS engine simulation presents an inverted velocity profile relative to the full scale engine. If the internal jet flow phenomena have little influence on the airframe this may not present difficulties.

Replicating the engine bypass exhaust properties with an engine simulator also connects with the inlet flow physics. In the case of air-turbine powered engine simulation the turbine drive-air intake occurs through an external supply rather than through the engine inlet. This leads to the fact that the engine simulator inlet mass flow rate (through the highlight area) is relatively too low by a factor F (core flow deficit), where

$$F = \frac{1}{1 + \frac{1}{BPR}}$$

since only the bypass flux is taken in through the inlet. This in turn generates a difference in the inlet pressure field with respect to the full

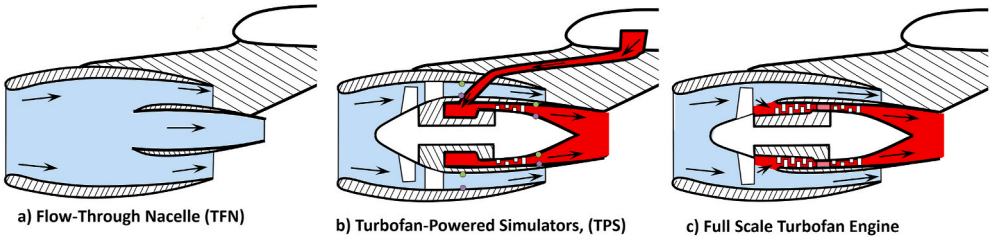

Fig. 20. Illustration of a flow-through nacelle, an air-turbine powered simulator (TPS) and a turbofan engine. Taken from Ref. [152].

scale. Increasing bypass ratio reduces this issue bringing F closer unity. A particular solution to restore the inlet pressure coefficient distribution is by contracting the TPS inlet relative to the full-scale engine. The inlet shape is modified such that the pressure coefficient distribution on the inlet is recovered for a certain engine operating point. Laban [154] reported the inlet shape modification using optimisation of the coefficients of a sum of shape functions parameterising the radial decrease and a cost function which was the sum of squared differences of the pressure coefficients distributions of the engine simulator inlet and the full scale engine inlet.

4.2. Thrust and drag bookkeeping

The simulator thrust itself is not a simulation parameter, however it must be accurately known for thrust and drag bookkeeping to determine engine installation effects. To this purpose, different configurations i.e. with engine(s) installed (wing-body-pylon-nacelle) and without engine (s) installed (wing-body) are applied in the wind tunnel. The installation drag is then assessed as the difference between these configurations:

$$\Delta D_i = D_{WBPN} - D_{WB}.$$

Von Geyr [155] discussed the determination of these installation effect and also points out a further separation between pure installation (power-off) and power (jet) effects.

Installation effects = [WingBody + Pylon + Engine at reference point] - WingBody

Power effects = [WingBody + Pylon + Engine at operating point] - [WingBody + Pylon + Engine at reference point]

The reference point in the previous is the idle or flow-through nacelle operating point. The corresponding drag coefficients in the above are summed to obtain the total installation drag coefficient which typically amounts to 10-20 drag counts for a twin-engine transport aircraft at cruise (for a total drag coefficient of typically $C_d = 0.020 - 0.030$ (200–300 drag counts)).

In general the wind tunnel main (strain gauge) balance measures the overall forces and moments occurring on the model configuration. The drag of the wing-body configuration can therefore be measured directly, but the drag of wing-body-pylon-nacelle configuration is not directly accessible since the balance registers the combination of forces on the airframe and the net propulsive force of the simulator (transmitted through the pylon). At this point it becomes important to set up a thrust and drag bookkeeping scheme decomposing the complete domain and assign contributions to either thrust or drag. In the case where engine and airframe can be reasonably well separated this decomposition traditionally defines the thrust domain to consist of the pre-entry streamtube (extending from infinitely far upstream), the engine internal flow and the post-exit stream tube (extending to infinitely far downstream). Contributions outside this domain (airframe, external nacelle, etc.) are attributed to drag [63]. As a consequence pressure and friction forces on the core cowl and the plug are accounted as thrust (this also goes for the pylon section immersed in the bypass flow). Fig. 21 shows the decomposition into thrust and drag domains.

The net propulsive force (F_{np}) transmitted through the pylon (cutting the control volume) induced by the simulator in the wind tunnel (X_W in the figure of [155]) is then written as the result of the momentum fluxes, the pressure and friction forces on the inlet plane, the external nacelle, the core and bypass exhaust exit planes and the cowling parts immersed in the exhaust flow. Application of momentum conservation on the pre-entry and post-exit stream tube volumes allow the net propulsive force transmitted through the pylon to be written as

$$F_{np} = m_{18}u_{19} + m_8u_9 - m_1u_0 - \left(\varphi_{pre} + \varphi_{ext} + \varphi_{post}\right).$$

The φ-terms are integrals of the pressure (difference) and the friction over the pre-entry stream tube, the external nacelle and the post-exit stream tube surfaces. This net propulsive force includes both thrust and drag terms.

The gross thrust in the calibration facility is formed by the exhaust jet momenta (infinitely far downstream) and the post-exit streamtube force. The standard bookkeeping procedure tracks gross thrust values using discharge and velocity coefficients describing the deviation from ideal (isentropic) behaviour. A starting point for the determination of the engine simulator calibration coefficients is the assumption that they are principally dependent on the total-to-static (nozzle) pressure ratio (FNPR) and the relation is calibrated as such. The replication of the wind tunnel flow ram pressure ratio produces the equivalent wind tunnel flow Mach number. This can be accomplished through a special mounting of the isolated engine simulator in a controllable low-pressure vessel, called Engine Calibration Facility (ECF). Such a setup is shown in Fig. 22.

This setup presents ambient total pressure and temperature conditions at the engine simulator inlet and a controllable static pressure at the exhaust. The controllable static pressure is realized by a large capacity pumping system connected to the downstream end of the tank. Lowering of the exhaust static pressure presents a higher equivalent wind tunnel flow Mach number. The isolated engine simulator is mounted to a six-component strain-gauge balance allowing the registration of the forces and moments occurring on the isolated engine simulator. The interface between the low-pressure vessel front and the

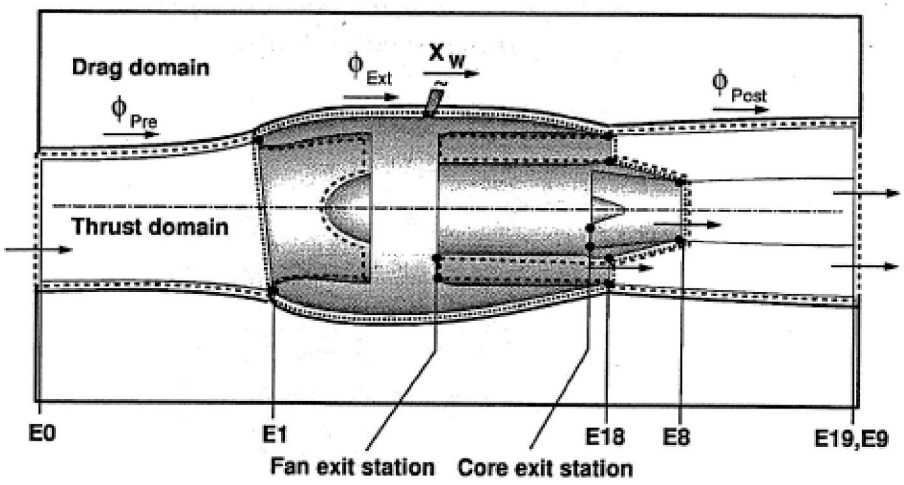

Fig. 21. Domain decomposition for thrust and drag bookkeeping. Taken from Ref. [155].

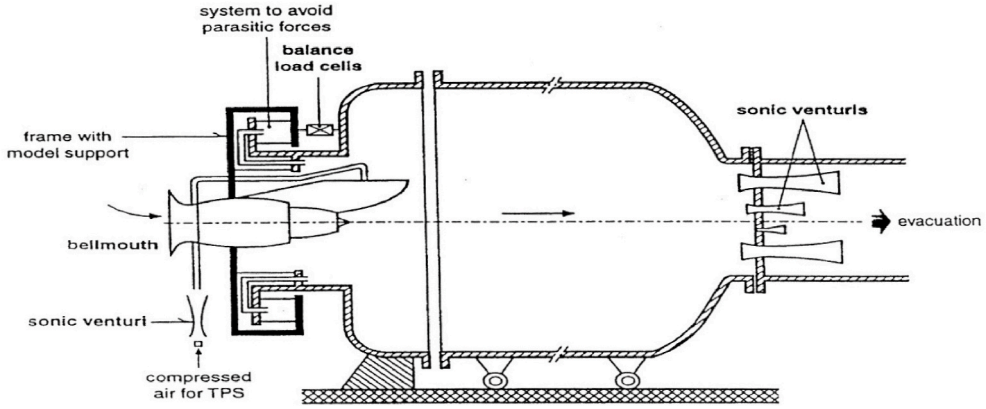

Fig. 22. Sketch of the engine calibration facility (ECF) at German-Dutch wind tunnels (DNW).

engine simulator is an S-shaped rubber seal allowing for an air-tight sealing without presenting parasitic loads to the strain-gauge balance. A compensation mechanism avoids the remainder of net pressure differences on the seal. The isolated engine simulator is equipped with a bellmouth inlet, that serves to determine the inlet mass flow rate and presents uniform, distortion-free flow to the fan face and minimizes inlet total pressure losses. An air-turbine driven simulator is connected to a pressure and temperature controlled air supply line which crosses the strain-gauge balance using flexible couplings to avoid parasitic loads. The supply mass flow rate is measured through the use of a venturi in the sonic (choked) state. The low-pressure vessel is also equipped with venturis in the downstream end. The venturis can be individually opened or closed. This allows the determination of the mass flow rate exiting the low-pressure vessel as well. The calibration facility can be run in two modes. One mode is when the downstream end Venturis are choked, in which case there is limited vessel pressure control; another mode is when the downstream end Venturis are unchoked, in which case there is full control over the vessel pressure. Prior to engine simulator calibration the bellmouth inlet mass flow rate as a function of pressure ratio is calibrated with the low-pressure vessel downstream Venturis in choked mode. These calibrated Venturis present accurate mass flow rates. The calibration results in a bellmouth discharge coefficient C_d^{BM} function which equals the fraction of the calculated isentropic bellmouth mass flow rate and the actual mass flow rate. The isentropic bellmouth mass flow rate calculations are accomplished through the use of static pressure taps in the bellmouth throat and total pressure and temperature stations at its inlet plane. Typical accuracies on gross thrust values are 0.2–0.3% of the full thrust value [153,156]. Procedure descriptions can be found in Refs. [157–160].

With the gross thrust calibrated a thrust and drag separation can be made to assess the drag of the powered configuration. The experimentally obtainable installation drag can then be written

$$\Delta D_i = D_{WBPE} - D_{WB},$$

$$= \varphi_{pre} + \varphi_{ext} + \Delta D_{AC}.$$

The ΔD_{AC} term is the change in drag over the aircraft (wing-body) surfaces due to the installation. The viscous drag contribution in the pre-entry drag term φ_{pre} is negligible so that only the pressure integral over the pre-entry stream tube remains which is also termed *additive* drag. The additive drag together with the pressure contribution in φ_{ext} (external nacelle pressure distribution) is termed the *spillage* drag [161].

Both De Wolf [153] and Von Geyr [155] pointed out some shortcomings of the basic form of the thrust and drag bookkeeping scheme. The first point entails that upon moving from the calibration facility to the wind tunnel test section the presence of external flow and the proximity of the airframe can present different exhaust conditions. Specifically the local static pressure level at the exhaust exit plane can be slightly different from the free stream value infinitely far downstream. This leads to the effect of flow suppression i.e. a reduced mass flow rate and a decreased local nozzle pressure ratio. Secondly the post-exit stream tube shape itself can differ in the wind tunnel section relative to the static calibration leading to changes in the post-exit force. Moreover surfaces previously contained in the thrust domain during static calibration may have moved to the drag domain or vice versa. Modified exhaust conditions may in turn affect upstream conditions.

Sabater [152] proposed possible improvements of the basic wind tunnel TDB by considering the post-exit force and re-expressing the FNPR as the ratio between the total pressure at fan nozzle outlet and the actual average static pressure at the same position, rather than the freestream static pressure. This difference is larger when considering installed engines, in which the wing presence is known to increase the back-pressure, compared to isolated conditions. This issue emerges in particular for UHBPR engines due to the close coupling to the airframe. With a standard calibration, the mentioned effects might be lost, the gross thrust being considered independent of the external flow field.

4.3. Supplemental

Burgsmuller [162] presented a general and qualitative overview of TPS testing. Some accuracy aspects were mentioned. A highlighted item in the paper was thrust vector deviations from the engine centre line. The deviation was stated to be geometry dependent and be easily mistaken for aerodynamic effects. The paper also highlighted ground plane effects that account for lift and pitching moment increases. In an early paper from Hall [163] and a later study from Mikkelsen [164], functional dependencies for discharge and thrust coefficients were discussed for long radius ASME nozzles and Venturi ducts. The papers recommended future research into more representative nozzles or engines. Mikkelsen in Ref. [165] presented experimental performance data for the discharge and thrust coefficients for the AIAA dual separate flow reference nozzle. Comparisons with CFD were drawn as well. CFD to experiment differences ran from 0.35% to 0.67% for the discharge coefficients, where engine manufacturers and wind tunnel testing typically requires 0.3% or less, and up to 0.03% for the thrust coefficients. The paper concluded that CFD and experimental results were complementary and that both are required for effective performance determinations.

Wright [166] demonstrated statistical error analysis of the velocity coefficient of a flow-through nacelle. A global third order fit (as a function of equivalent Mach number) was deemed sufficient. The importance of a curve fit was stressed by pointing out that the curve confidence intervals are smaller than those for the means of individual samples. Yoder [167] and Dippold [168] summarised results obtained for an AIAA workshop on propulsion aerodynamics. A comparison was drawn between experiments and CFD for discharge and thrust

coefficients of different types of (mostly conical) convergent nozzles and also an S-duct. One of the conical nozzles was also equipped with a splitter plate. Different turbulence models and grid sizes were used. CFD and experiment matched quite well for discharge coefficients. Thrust coefficients still showed differences of 1% or larger. Shock locations were also predicted rather well although finer grids were recommended to better resolve the shock structure. In addition static pressure and rake data were compared. A similar study was performed earlier by Thornock [169] comparing experiment and analytical expressions. Harris [156] described wind tunnel testing with TPS technology over the course of time. Various rigs, models and technological advances are described.

Von Geyr [155] proposed precise definitions of engine simulator calibration coefficients in wind tunnel experiments and numerical computations (CFD). In addition perturbing effects on these coefficients from the external flow were discussed, and corrections proposed. These efforts were validated using wind tunnel data acquired in the EU ENIFAIR program with three different engine simulators having increasing bypass ratio. The external flow Mach number was identified as being important in the thrust bookkeeping. Jet spreading and flow recompression effects led to post-exit pressure increase. This presented increased (unaccounted) gross thrust with higher external flow Mach numbers. For free flow Mach numbers below 0.25 the effect did not need to be taken into account. Burgsmuller [116] presented an overview of the work carried out in past European framework programmes. Three engine types namely a conventional turbofan, a VHBR and an UHBR engines were considered, as well as their positioning. Wind tunnel testing and CFD were performed in these efforts. The results showed that lift loss and drag increase due to engine installation become larger with increasing bypass ratio. McCall [170] highlighted some key results of wind tunnel tests with high bypass ratio engine nacelles in various configurations and sizes. Among other qualitative points, installation and interference drag trend lines as a function of fan diameter were presented. Installed testing included only flow-through nacelles.

Doornbos [171] presented an overview of TPS testing procedures in the wind tunnel to obtain interference drag values for half-models. A comparison with blown nacelles was drawn as well. Tompkins [172] described a relatively modest modification of exhaust nozzles of an existing TPS unit to move from low bypass, high fan pressure ratio simulation to high bypass, low fan pressure ratio simulation. Isolated unit test results were presented. Hoheisel [161] discussed essential engine simulation parameters and focused on the thrust ratio (fan to turbine thrust) which typically receives less attention in the literature. Turbine powered simulator and full scale engine thrust ratios generally do not coincide. The article analysed the influence of thrust ratio on drag behaviour using theory, CFD and wind tunnel experiments conducted in the EU programs ENIFAIR (engine integration on future transport aircraft), DUPRIN (ducted propfan investigations) and AIRDATA (aircraft drag and thrust analysis). The authors also stressed the importance of TPS testing because of the jet effects on the drag behaviour of aircraft configuration. Drag coefficient value increases with bypass ratio were presented and came close to 4% for UHBR engines relative to the wing-body configuration. The paper concluded that the thrust ratio is of no importance on the drag behaviour in cruise condition.

Welge [173] described in quite some detail a TPS testing procedure for installed testing of the DC-10 aircraft with an intermediate wind-on assessment of the isolated engine simulator. Shea [174] reported a turbine powered engine simulation on a blended-wing-body aircraft in NASA's NFAC. TPS calibration strategies were described together with propulsion-airframe integration results. Different control surface configurations were tested and also two heights of the engine simulators with respect to the airframe. The design and fabrication of this wind tunnel model were detailed in Refs. [175].

In conclusion, wind tunnel testing of installed engines through turbo-powered simulators has been an essential stage of aircraft development and has contributed to the successful improvement of aircraft performance. The vast experience acquired will be determinant for an accurate simulation of future UHBPR engines, for which, however, some modifications of current practices might be devised. Areas of interest can regard a more careful evaluation of the sensitivity of calibration coefficients with respect to the external flow field, the possibility of using a more complete thrust/drag bookkeeping procedure, the TPS mass flow deficit effect on installation drag, the influence of non-duplicated core flow, and the possibility of building different engine simulator concepts based on electric-driven fan.

5. Conclusion

A series of challenges related to full exploitation of UHBRP engines has been presented, pointing out first how the increase of propulsive efficiency affects engine cycle design. The search for low specific thrust requires higher bypass mass flow rate and reduced fan pressure ratio, directly impacting the power split between engine components and its overall size. On the internal side, the need for a geared turbofan or variable geometry parts to allow matching of diverging requirements between engine components or sufficient margin from stall increases the complexity and weight of the propulsor. On the external side, novel nacelle geometric and installation technology is required to mitigate the appearance of distorted flow field over the wing and drag and weight penalty. The combination of low FPR, short intake, and unchoked nozzle, in addition, exacerbates the influence of boundary conditions on the engine working point, causing larger installed effects on engine matching. The progresses in computational modelling and power have allowed to develop accurate tools to quantify the installation effects and design the single components exploiting DOE and optimisation techniques for multi-objective problems. On the other hand, wind tunnel tests are still a building block of aircraft development and powered engine simulators are a complete way of reproducing flight conditions. However, in both fields a number of issues impose a discussion on the validity of standard practices, given the larger intersection between the domain of dependencies of the aircraft parts, that can be summarised in the correct implementation of boundary conditions. The studies on BLI propulsion push the development of adequate tools for prediction of engine response to ambient conditions and consistent thrust/drag bookkeeping, but even in classic underwing mounted engines this is becoming important in certain flight phases and possibly also when considering novel engine positioning. Similarly, in wind tunnel tests the assessment of the importance of parameters that cannot be duplicated should be revised, to confirm or update thrust extraction methods or calibration procedures, in line with CFD capabilities. In conclusion, the complexity of the interactions and their impact on the overall system performance invite to proceed towards closely coupled design and analysis methods, to allow full exploitation of the many benefits of UHBPR propulsive units.

Funding

This study is financed by the Clean Sky 2 project IVANHOE (Installed adVAnced Nacelle uHbr Optimisation and Evaluation). The project has received funding from the European Union's Horizon 2020 research and innovation programme under grant agreement number 863415.

Credit authorship contribution statement

Andrea Magrini: Literature research, Writing - Original draft preparation, Data analysis and curation. **Ernesto Benini:** Document review, Project Coordination. **Hua-Dong Yao:** Literature research, Writing - Original draft preparation, Document review, Project Coordination. **Jos Postma:** Literature research, Writing - Original draft preparation. **Chris Sheaf:** Document review.

Declaration of competing interest

The authors declare that they have no known competing financial interests or personal relationships that could have appeared to influence the work reported in this paper.

References

[1] IATA, IATA Vision 2050, Technical Report, IATA, Singapore, 2011, https://doi.org/10.4271/640544. URL:.

[2] E. Commission, A vision for 2020, Technical Report, European Commission, Luxembourg, https://doi.org/10.2172/6980055, 2001.

[3] European Commission, FlightPath 2050, Technical Report, ACARE, Luxembourg, 2011, https://doi.org/10.2777/50266. URL: https://ec.europa.eu/transport/sites/transport/files/modes/air/doc/flightpath2050.pdf.

[4] W.R. Graham, C.A. Hall, M. Vera Morales, The potential of future aircraft technology for noise and pollutant emissions reduction, Transport Pol. 34 (2014) 36–51.

[5] C.E. Hughes, Aircraft engine technology for green aviation to reduce fuel burn, in: 3rd AIAA Atmospheric Space Environments Conference, American Institute of Aeronautics and Astronautics, Reston, Viriginia, 2011, https://doi.org/10.2514/6.2011-3531. URL: http://arc.aiaa.org/doi/10.2514/6.2011-3531.

[6] H. Hoheisel, Aerodynamic aspects of engine-aircraft integration of transport aircraft, Aero. Sci. Technol. 1 (1997) 475–487.

[7] W. Lu, G. Huang, X. Xiang, J. Wang, Y. Yang, Thermodynamic and aerodynamic analysis of an air-driven fan system in low-cost high-bypass-ratio turbofan engine, Energies 12 (2019) 1917.

[8] H. Yoshihara, AGARD Rep. No 712 Special Course on Subsonic/transonic Aerodynamic Interference for Aircraft, Technical Report, AGARD, Neuilly-sur-Seine, 1983.

[9] R. Rudnik, C.C. Rossow, H.F.V. Geyr, Numerical simulation of engine/airframe integration for high-bypass engines, Aero. Sci. Technol. 6 (2002) 31–42.

[10] J. Borradaile, Towards the optimum ducted UHBR engine, in: 24th Joint Propulsion Conference, American Institute of Aeronautics and Astronautics (AIAA), Boston, MA, 1988, https://doi.org/10.2514/6.1988-2954. URL:.

[11] R.A. Zimbrick, J.L. Colehour, Investigation of very high bypass ratio engines for subsonic transports, J. Propul. Power 6 (1990) 490–496.

[12] G. Krishnan, C.A. Perullo, D.N. Mavris, An assessment of relative technology benefits of a variable pitch fan and variable area nozzle, in: 49th AIAA/ASME/SAE/ASEE Joint Propulsion Conference, American Institute of Aeronautics and Astronautics, Reston, Virginia, 2013, https://doi.org/10.2514/6.2013-3604. URL: http://arc.aiaa.org/doi/10.2514/6.2013-3604.

[13] B.G. McKay, Next generation propulsion & air vehicle considerations, in: 45th AIAA/ASME/SAE/ASEE Joint Propulsion Conference and Exhibit, American Institute of Aeronautics and Astronautics, Reston, Viriginia, 2009, https://doi.org/10.2514/6.2009-4803. URL: http://arc.aiaa.org/doi/abs/10.2514/6.2009-4803.

[14] R. Schnell, D. Schönweitz, M. Theune, J. Corroyer, Integration- and intake-induced flow distortions and their impact on aerodynamic fan performance, in: R. Radespiel, R. Niehuis, N. Kroll, K. Behrends (Eds.), Notes on Numerical Fluid Mechanics and Multidisciplinary Design, vol. 131, Springer, Cham, 2016, pp. 251–269, https://doi.org/10.1007/978-3-319-21127-5_15. URL: http://link.springer.com/10.1007/978-3-319-21127-5{_}15.

[15] A. Guha, Optimum fan pressure ratio for bypass engines with separate or mixed exhaust streams, J. Propul. Power 17 (2001) 1117–1122.

[16] J. Kurzke, I. Halliwell, Propulsion and Power: an Exploration of Gas Turbine Performance Modeling, Springer International Publishing, 2018, https://doi.org/10.1007/978-3-319-75979-1.

[17] G.H. Wright, J.G. Russell, M. 45SD-02 variable pitch geared fan engine demonstrator test and evaluation experience, Aeronaut. J. 84 (1980) 268–277.

[18] Pratt & Whitney, Pratt & Whitney geared turbofan, URL: https://pwgtf.com/https://pwgtf.com/benefits/, 2019.

[19] Rolls-Royce, Advance and UltraFan® – Rolls-Royce, 2019. URL: https://www.rolls-royce.com/media/our-stories/innovation/2016/advance-and-ultrafan.aspx{#}application.

[20] A. Geer, Clean sky 2 - next stages in bringing vhbr technology to life: ultrafan® - vhbr engine - advance3 engine, in: E.C. H2020 (Ed.), Tandem Aerodays 2019, 2019. URL: http://www.tandemaerodays19-20.eu/wp-content/themes/tandem/presentations/A2.zip.

[21] R. Christie, Propulsion System Integration and Modelling Synthesis, Phd Thesis, University of Cranfield, 2016.

[22] J. Felder, H. Kim, G. Brown, Turboelectric distributed propulsion engine cycle analysis for hybrid-wing-body aircraft, URL: https://arc.aiaa.org/doi/abs/10.2514/6.2009-1132, 2009 https://arc.aiaa.org/doi/pdf/10.2514/6.2009-1132.

[23] C.A. Hall, D. Crichton, Engine design studies for a silent aircraft, J. Turbomach. 129 (2006) 479–487.

[24] L. Larsson, T. Grönstedt, K.G. Kyprianidis, Conceptual design and mission analysis for a geared turbofan and an open rotor configuration, in: Aircraft Engine; Ceramics; Coal, Biomass and Alternative Fuels; Wind Turbine Technology of *Turbo Expo: Power For Land, Sea, and Air*, ume vol. 1, 2011, pp. 359–370. URL: https://doi.org/10.1115/GT2011-46451. arXiv: https://asmedigitalcollection.asme.org/GT/proceedings-pdf/GT2011/54617/359/2756082/359_1.pdf.

[25] B.K. Kestner, J.S. Schutte, J.C. Gladin, D.N. Mavris, Ultra high bypass ratio engine sizing and cycle selection study for a subsonic commercial aircraft in the N+2 timeframe, in: Proceedings of the ASME Turbo Expo, vol. 1, American Society of Mechanical Engineers (ASME), 2011, pp. 127–137, https://doi.org/10.1115/GT2011-45370.

[26] K. Aloyo, C.A. Perullo, D.N. Mavris, An assessment of ultra high bypass engine architecture and installation considerations, in: 50th AIAA/ASME/SAE/ASEE Joint Propulsion Conference 2014, American Institute of Aeronautics and Astronautics Inc., 2014, https://doi.org/10.2514/6.2014-3685.

[27] X. Yang, H. Tang, M. Chen, Performance modeling and optimization assessment of variable pitch fan for ultrafan engine, in: 2018 Joint Propulsion Conference, American Institute of Aeronautics and Astronautics Inc, AIAA, 2018, https://doi.org/10.2514/6.2018-4400.

[28] D.L. Daggett, S.T. Brown, R.T. Kawai, Ultra-efficient Engine Diameter Study, Technical Report, NASA, 2003. URL: https://ntrs.nasa.gov/search.jsp?R=20030061085.

[29] J. Bijewitz, A. Seitz, M. Hornung, E. Luftfhart Bauhaus, Architectural comparison of advanced ultra-high bypass ratio turbofans for mesium to long range application, in: Deutscher Luft- und Raumfhahrtkongress 2014, DLR, 2014, p. 12. URL: http://www.dglr.de/publikationen/2015/340105.pdf.

[30] J.J. Berton, M. Guynn, Multi-objective optimization of turbofan design parameters for an advanced, single-aisle transport, AIAA (2010) 1–17.

[31] M.D. Guynn, J.J. Berton, K.L. Fisher, W.J. Haller, M.T. Tong, D.R. Thurman, Refined Exploration of Turbofan Design Options for an Advanced Single-Aisle Transport, Technical Report, NASA, 2011. URL: https://ntrs.nasa.gov/search.jsp?R=20110004165.

[32] D. Giesecke, M. Lehmler, J. Friedrichs, J. Blinstrub, L. Bertsch, W. Heinze, Evaluation of ultra-high bypass ratio engines for an over-wing aircraft configuration, J. Global Power and Propulsion Soc. 2 (2018) 493–515.

[33] ENOVAL Consortium, ENOVAL Technology Brochure, Technical Report, EIMG, 2018. URL: www.enoval.eu.

[34] M. Albert, D. Bestie, Aerodynamic design optimization of nacelle and intake, in: Proceedings of the ASME Turbo Expo, vol. 2, American Society of Mechanical Engineers Digital Collection, 2013, https://doi.org/10.1115/GT2013-94857.

[35] B.M. Kulfan, Universal parametric geometry representation method, J. Aircraft 45 (2008) 142–158, https://doi.org/10.2514/1.29958.

[36] R. Christie, A. Heidebrecht, D. MacManus, An automated approach to nacelle parameterization using intuitive class shape transformation curves, J. Eng. Gas Turbines Power 139 (2017).

[37] M. Robinson, D.G. Macmanus, K. Richards, C. Sheaf, Short and slim nacelle design for ultra-high BPR engines, in: AIAA SciTech Forum - 55th AIAA Aerospace Sciences Meeting, American Institute of Aeronautics and Astronautics Inc., 2017, https://doi.org/10.2514/6.2017-0707.

[38] F. Tejero, M. Robinson, D.G. MacManus, C. Sheaf, Multi-objective optimisation of short nacelles for high bypass ratio engines, Aero. Sci. Technol. 91 (2019) 410–421.

[39] F. Tejero, I. Goulos, D. MacManus, C. Sheaf, Effects of Aircraft Integration on Compact Nacelle Aerodynamics, American Institute of Aeronautics and Astronautics (AIAA), 2020, https://doi.org/10.2514/6.2020-2225.

[40] X. Fang, Y. Zhang, H. Chen, Transonic nacelle aerodynamic optimization based on hybrid genetic algorithm, in: 17th AIAA/ISSMO Multidisciplinary Analysis and Optimization Conference, American Institute of Aeronautics and Astronautics Inc, AIAA, 2016, https://doi.org/10.2514/6.2016-3833.

[41] A. Heidebrecht, D.G. MacManus, Surrogate model of complex non-linear data for preliminary nacelle design, Aero. Sci. Technol. 84 (2019) 399–411.

[42] B. Hodder, An Investigation of Engine Influence on Inlet Performance(conducted in the Ames 40- by 80-foot Wind Tunnel), NASA, Seattle, WA, 1981. Technical Report.

[43] S. Schulze, Experimental Investigations on the Vortex Dynamics of a Stalling Jet Engine Inlet, Phd Thesis, Universität der Bundeswehr München, 2013.

[44] S.D. Erbslöh, W.J. Crowthert, J.R. Frutos, Control of compressor face total pressure distortion on a high bypass turbofan intake using air-jet vortex generators, in: 2nd AIAA Flow Control Conference, American Institute of Aeronautics and Astronautics, Reston, Viriginia, 2004, https://doi.org/10.2514/6.2004-2206. URL: http://arc.aiaa.org/doi/10.2514/6.2004-2206.

[45] S. Übelacker, R. Hain, C.J. Kähler, Flow investigations in a stalling nacelle inlet under disturbed inflow, Notes on Num. Fluid Mech. Multidisciplinary Des. 131 (2016) 271–283.

[46] D.L. Motycka, Reynolds number and fan/inlet coupling effects on subsonic transportinlet distortion, J. Propul. Power 1 (1985) 229–234.

[47] M.J. Larkin, P.S. Schweige, Ultra High Bypass Nacelle Aerodynamics, NASA, 1992. Technical Report.

[48] S. Kennedy, T. Robinson, S. Spence, J. Richardson, Computational investigation of inlet distortion at high angles of attack, J. Aircraft 51 (2014) 361–376.

[49] T. Cao, N.R. Vadlamani, P.G. Tucker, A.R. Smith, M. Slaby, C.T. Sheaf, Fan-Intake interaction under high incidence, J. Eng. Gas Turbines Power 139 (2017).

[50] A. Burlot, F. Sartor, M. Vergez, M. Méheut, R. Barrier, Method comparison for fan performance in short intake nacelle, in: 2018 Applied Aerodynamics Conference, American Institute of Aeronautics and Astronautics, Reston, Virginia, 2018, https://doi.org/10.2514/6.2018-4204. URL: https://arc.aiaa.org/doi/10.2514/6.2018-4204.

[51] M. Méheut, F. Sartor, M. Vergez, M. Laban, R. Schnell, A. Stuermer, G. Lefevre, Assessment of fan/airframe aerodynamic performance using 360° uRANS computations: code-to-code comparison between ONERA, DLR, NLR and airbus, in: AIAA Scitech 2019 Forum, American Institute of Aeronautics and Astronautics Inc, AIAA, 2019, https://doi.org/10.2514/6.2019-0582.

[52] A. Stuermer, DLR TAU-code uRANS turbofan modeling for aircraft aerodynamics investigations, Aerospace 6 (2019) 121.

[53] D. Schoenweitz, M. Theune, R. Schnell, Inlet distortion sensitivity of fans with different pressure ratios, in: ISABE-2015, 2015.

[54] A. Peters, Z.S. Spakovszky, W.K. Lord, B. Rose, Ultra-short nacelles for low fan pressure ratio propulsors, in: Proceedings of the ASME Turbo Expo, 1A, American Society of Mechanical Engineers Digital Collection, 2014, https://doi.org/10.1115/GT2014-26208. URL: https://asmedigitalcollection.asme.org/turbomachinery/article/doi/10.1115/1.4028235/378472/Ultrashort-Nacelles-for-Low-Fan-Pressure-Ratio.

[55] J. Corroyer, R. Schnell, Coupled Fan and Intake Design Optimization for Installed UHBR-Engines with Ultra-short Nacelles, 2015.

[56] G. Yu, D. Li, Y. Shu, Z. Zhang, Numerical simulation for engine/airframe interaction effects of the bwb300 on aerodynamic performances, Int. J. Aerospace Eng. 2019 (2019) 1072196.

[57] D.L. Rodriguez, Multidisciplinary optimization method for designing boundary-layer- ingesting inlets, J. Aircraft 46 (2009) 883–894.

[58] H. Kim, M.S. Liou, Shape design optimization of embedded engine inlets for N2B hybrid wing-body configuration, Aero. Sci. Technol. 30 (2013) 128–149.

[59] H. Kim, M.S. Liou, Flow simulation and optimal shape design of N3-X hybrid wing body configuration using a body force method, Aero. Sci. Technol. 71 (2017) 661–674.

[60] W. Thollet, G. Dufour, X. Carbonneau, F. Blanc, Assessment of body force methodologies for the analysis of intake-fan aerodynamic interactions, in: Proceedings of the ASME Turbo Expo, 2C-2016, American Society of Mechanical Engineers, 2016, https://doi.org/10.1115/GT2016-57014. URL: https://asmedigitalcollection.asme.org/GT/proceedings/GT2016/49712/Seoul, SouthKorea/236620.

[61] B. Godard, E. De Jaeghere, N. Ben Nasr, J. Marty, R. Barrier, N. Gourdain, Methodologies for turbofan inlet aerodynamics prediction, in: 35th AIAA Applied Aerodynamics Conference, 2017, American Institute of Aeronautics and Astronautics Inc, AIAA, 2017, https://doi.org/10.2514/6.2017-3413.

[62] B. Godard, E. de Jaeghere, N. Gourdain, Efficient design investigation of a turbofan in distorted inlet conditions, in: Proceedings of the ASME Turbo Expo, 2A-2019, American Society of Mechanical Engineers (ASME), 2019, https://doi.org/10.1115/GT2019-90471.

[63] MIDAP Study group, Guide to In-Flight Thrust Measurement of Turbo- Jets and Fan Engines, AGARD, London, 1979. Agardograph No. 237, Technical Report No. AG-237, Technical Report.

[64] D. DUSA, D. Lahti, D. Berry, Investigation of Subsonic Nacelle Performance Improvement Concept, American Institute of Aeronautics and Astronautics (AIAA), 1982, https://doi.org/10.2514/6.1982-1042.

[65] Y. Zhang, H. Chen, S. Fu, M. Zhang, M. Zhang, Drag prediction method of powered-on civil aircraft based on thrust drag bookkeeping, Chin. J. Aeronaut. 28 (2015) 1023–1033.

[66] R.L. Thornock, Comparison of Participant Analyses with Experimental Results for Conical Nozzle Flowfields and Performance, American Institute of Aeronautics and Astronautics (AIAA), 2013, https://doi.org/10.2514/6.2013-3735.

[67] N.D. Domel, Perspectives on Propulsion CFD for Nozzle Applications Relevant to the AIAA Propulsion Aerodynamics Workshop, AIAA, 2015, https://doi.org/10.2514/6.2015-3778. URL: https://arc.aiaa.org/doi/abs/10.2514/6.2015-3778.

[68] R.L. Thornock, Propulsion AerodynamicWorkshop II, Summary of Participant Results for a Dual Separate Flow Reference Nozzle, Including Some Experimental Results, American Institute of Aeronautics and Astronautics (AIAA), 2016, https://doi.org/10.2514/6.2016-4503.

[69] M.D. Christiansen, R.L. Thornock, Propulsion aerodynamic workshop III, performance analyses of a dual separate flow reference nozzle, dual confluent flow reference nozzle, and two single flow convergent nozzles, in: 53rd AIAA/SAE/ASEE Joint Propulsion Conference, 2017, American Institute of Aeronautics and Astronautics Inc, AIAA, 2017, https://doi.org/10.2514/6.2017-4659.

[70] R. Davy, C. Brossard, J. Jourdan, Y. Pioche, O. Piccin, Installation effects characterization of vhbpr engine part ii: experimental study using particle image velocimetry, AIAA paper, AIAA 3253 (2009) (2009).

[71] F. Dezitter, H. Bezard, X. de Saint Victor, K. Zeggai, K. Britchford, G. Joubert, G. Puigt, Installation effects characterization of vhbr engines part iii: cfd assessment for jet mixing, AIAA paper, AIAA 3370 (2009) (2009).

[72] J. Huber, M. Omais, A. Vuillemin, R. Davy, Characterization of Installation Effects for HBPR Engine, Part 4: Assessment of Jet Acoustics, 2009, https://doi.org/10.2514/6.2009-3371. URL: https://arc.aiaa.org/doi/abs/10.2514/6.2009-3371.

[73] A. Vuillemin, O. Piccin, R. Davy, Installation effects characterization of vhbr engines–part i: experimental setup and wind tunnel improvement, in: AIAA/CEAS Aeroacoustics Conference, AIAA, 2007.

[74] I. Goulos, T. Stankowski, J. Otter, D. MacManus, N. Grech, C. Sheaf, Aerodynamic design of separate-jet exhausts for future civil aero-engines - Part I: parametric geometry definition and computational fluid dynamics approach, J. Eng. Gas Turbines Power 138 (2016).

[75] I. Goulos, J. Otter, T. Stankowski, D. MacManus, N. Grech, C. Sheaf, Aerodynamic design of separate-jet exhausts for future civil aero-engines - Part II: design space exploration, surrogate modeling, and optimization, J. Eng. Gas Turbines Power 138 (2016).

[76] G. Giangaspero, D. MacManus, I. Goulos, Surrogate models for the prediction of the aerodynamic performance of exhaust systems, Aero. Sci. Technol. 92 (2019) 77–90.

[77] I. Goulos, D. MacManus, C. Sheaf, Civil turbofan engine exhaust aerodynamics: impact of fan exit flow characteristics, Aero. Sci. Technol. 93 (2019) 105181.

[78] J.J. Otter, R. Christie, I. Goulos, D.G. MacManus, N. Grech, Parametric design of non-axisymmetric separate-jet aero-engine exhaust systems, Aero. Sci. Technol. 93 (2019), 105186.

[79] W.J. Wang, L. Zhou, Z.X. Wang, J.W. Shi, The influence of exhaust system on the performance of the high bypass ratio turbofan engine nacelle, in: 2018 Joint Propulsion Conference, American Institute of Aeronautics and Astronautics Inc, AIAA, 2018, https://doi.org/10.2514/6.2018-4669.

[80] Z.N. Wang, J. Tyacke, P. Tucker, Large Eddy Simulation of Serration Effects on an Ultra-high-bypass-ratio Engine Exhaust Jet, 2018, https://doi.org/10.1016/j.crme.2018.07.003.

[81] J.C. Tyacke, Z.-N. Wang, P.G. Tucker, LES-RANS of installed ultra-high-bypass-ratio coaxial jet aeroacoustics with flight stream, AIAA J. 57 (2019) 1215–1236.

[82] A.E. Harris, K.C. Paliwal, Civil turbofan propulsion system integration studies using powered testing techniques at ARA, bedford, in: AIAA Paper, American Institute of Aeronautics and Astronautics, Reston, Virigina, 1984, pp. 74–98, https://doi.org/10.2514/6.1984-593. URL: http://arc.aiaa.org/doi/10.2514/6.1984-593.

[83] Sae, Advanced Ducted Propulsor In-Flight Thrust Determination AIR540, Technical Report, SAE International, Troy, Michigan USA, 2014.

[84] F. Tejero, I. Goulos, D. MacManus, C. Sheaf, Effects of Aircraft Integration on Compact Nacelle Aerodynamics, 2020, https://doi.org/10.2514/6.2020-2225. URL: https://arc.aiaa.org/doi/abs/10.2514/6.2020-2225 https://arc.aiaa.org/doi/pdf/10.2514/6.2020-2225.

[85] M. Robinson, D.G. MacManus, C. Sheaf, Aspects of aero-engine nacelle drag, Proc. IME G J. Aero. Eng. 233 (2019) 1667–1682.

[86] D. Destarac, J. Van Der Vooren, Drag/thrust analysis of jet-propelled transonic transport aircraft; Definition of physical drag components, Aero. Sci. Technol. 8 (2004) 545–556.

[87] Y. Fan, W. Li, Review of far-field drag decomposition methods for aircraft design, J. Aircraft 56 (2019) 11–21.

[88] A. Betz, A Method for the Direct Determination of Wing-Section Drag, NACA, 1925. Technical Report.

[89] B. Jones, Measurement of Profile Drag by the Pitot-Transverse Method, Technical Report, Aeronautical Research Council, Tec, 1936.

[90] E. Maskell, Progress towards a Method for the Measurement of the Components of the Drag of a Wing of Finite Span, RAE Technical Report No, 1972, p. 72232.

[91] K. Oswatitsch, Gas Dynamics, Academic Press, New York, US, 1956.

[92] M. Giles, R. Cummings, Wake integration for three-dimensional flowfield computations theoretical development, J. Aircraft 36 (1999) 357–365.

[93] J. Van der Vooren, J. Slooff, Cfd-based drag prediction: state-of-the-art, theory, prospects, in: AIAA (Ed.), Lecture Noise for AIAA Professional Studies Series on Drag Prediction and Measurement, 1990.

[94] K. Kusunose, J. Crowder, G. Miller, Installed powered engine effects on drag using a wake-integral method, URL: https://arc.aiaa.org/doi/abs/10.2514/6.2000-2400, 2000 https://arc.aiaa.org/doi/pdf/10.2514/6.2000-2400.

[95] L. Paparone, R. Tognaccini, Computational fluid dynamics-based drag prediction and decomposition, AIAA J. 41 (2003) 1647–1657.

[96] M. Lanzetta, B. Mele, R. Tognaccini, Advances in aerodynamic drag extraction by far-field methods, J. Aircraft 52 (2015) 1873–1886.

[97] D. Destarac, Spurious far-field-boundary induced drag in two-dimensional flow simulations, J. Aircraft 48 (2011) 1444–1455.

[98] D. Destarac, Investigating negative drag in grid convergence for two-dimensional euler solutions, J. Aircraft 48 (2011) 1468–1470.

[99] M. Ueno, T. Kohzai, S. Koga, H. Kato, K. Nakakita, N. Sudani, 80% scaled NASA Common Research Model wind tunnel test of JAXA at relatively low Reynolds number, in: 51st AIAA Aerospace Sciences Meeting Including the New Horizons Forum and Aerospace Exposition 2013, 2013, https://doi.org/10.2514/6.2013-493.

[100] R. Tognaccini, Drag computation and breakdown in power-on conditions, J. Aircraft 42 (2005) 245–252.

[101] D. Hue, Fifth drag prediction workshop: ONERA investigations with experimental wing twist and laminarity, J. Aircraft 51 (2014) 1311–1322.

[102] J.B. Vos, S. Sanchi, A. Gehri, DPW4 results using different grids including near-field/far-field drag analysis, in: AIAA Applied Aerodynamics Conference, vol. 1, American Institute of Aeronautics and Astronautics Inc., 2010, https://doi.org/10.2514/6.2010-4552.

[103] T. Sibilli, M. Savill, Computational fluid dynamics drag prediction and decomposition for propulsive system integration, in: Proceedings of the ASME Turbo Expo, vol. 1, American Society of Mechanical Engineers Digital Collection, 2011, pp. 257–264, https://doi.org/10.1115/GT2011-46214.

[104] M. Ueno, K. Yamamoto, K. Tanaka, M. Murayama, R. Tognaccini, Far-field drag analysis of NASA common research model simulations by JAXA, in: 20th AIAA Computational Fluid Dynamics Conference 2011, 2011, https://doi.org/10.2514/6.2011-3699.

[105] Y. Deng, Y. Zhang, H. Chen, Drag prediction and decomposition of a real aircraft based on middle-field and far-field methods, in: 7th European Conference for Aeronautics and Space Cences C, 2017.

[106] A. Arntz, Civil Aircraft Aero-Thermo-Propulsive Performance Assessment by an Exergy Analysis of High-Fidelity CFD-RANS Flow Solutions, Phd thesis, Université de Lille 1, 2014. URL: https://hal.archives-ouvertes.fr/tel-01113135.

[107] Y.A. Cengel, M.A. Boles, Thermodynamics : an Engineering Approach, McGraw-Hill, 2011.

[108] M.A. Aguirre, S. Duplaa, X. Carbonneau, A. Turnbull, A Systematic Analysis of the Mechanical Exergy of an Airfoil by Using Potential Flow, euler and rans, 2019.

[109] M.A. Aguirre, S. Duplaa, Exergetic drag characteristic curves, AIAA J. 57 (2019) 2746–2757.

[110] K. Kusunose, S. Maruyama, A. Sasoh, A Wake Integration Method for Airplane Drag Prediction, Tohoku University Press, Sendai Japan, 2005.
[111] J.Z. Wu, X.Y. Lu, L.X. Zhuang, Integral force acting on a body due to local flow structures, J. Fluid Mech. 576 (2007) 265–286.
[112] C. Marongiu, R. Tognaccini, M. Ueno, Lift and lift-induced drag computation by lamb vector integration, AIAA J. 51 (2013) 1420–1430.
[113] B. Mele, M. Ostieri, R. Tognaccini, Vorticity based breakdown of the aerodynamic force in three-dimensional compressible flows, AIAA J. 54 (2016) 1198–1208.
[114] G. Oliveira, L.G. Trapp, A. Puppin-Macedo, Engine-airframe integration methodology for regional jet aircrafts with underwing engines, in: 41st Aerospace Sciences Meeting and Exhibit, American Institute of Aeronautics and Astronautics, Reston, Viriginia, 2003, https://doi.org/10.2514/6.2003-934. URL: http://arc.aiaa.org/doi/10.2514/6.2003-934.
[115] A.W. Chen, E.N. Tinoco, PAN AIR applications to aero-propulsion integration, J. Aircraft 21 (1984) 161–167.
[116] W. Burgsmüller, H. Hoheisel, Enifair — EU research into engine integration on future transport aircraft, Air Space Eur. 2 (2000) 81–85.
[117] C.C. Rossow, J.L. Godard, H. Hoheisel, V. Schmitt, Investigations of propulsion integration interference effects on a transport aircraft configuration, J. Aircraft 31 (1994) 1022–1030.
[118] C. Rossow, H. Hoheisel, Numerical study of interference effects of wing-mounted advanced engine concepts, in: ICAS 1994, ICAS, Anahaim, USA, 1994, pp. 1272–1282. URL: https://www.icas.org/ICAS{_}ARCHIVE/ICAS1994/ICAS-94-6.4.1.pdf.
[119] W. Burgsmüller, H. Hoheisel, J.W. Kooi, Engine/airframe interference on transport aircraft with ducted propfans - the European research program DUPRIN. ICAS 1994, ICAS, Anaheim, USA, 1994, pp. 2383–2399. URL: https://www.icas.org/ICAS{_}ARCHIVE/ICAS1994/ICAS-94-3.7.1.pdf.
[120] W. Burgsmüller, C. Rolllin, C.C. Rossow, Engine integration on future transport aircraft - the European research programs DUPRIN/ENIFAIR, in: ICAS 1998, ICAS, Melbourne, Australia, 1998. ICAS–98–5.6.1. URL: http://www.icas.org/ICAS{_}ARCHIVE/ICAS1998/PAPERS/561.PDF.
[121] O. Brodersen, Drag prediction of engine-airframe interference effects using unstructured Navier-Stokes calculations, J. Aircraft 39 (2002) 927–935.
[122] NASA, Nasa DPW, URL: https://aiaa-dpw.larc.nasa.gov/, 2020.
[123] J. Vassberg, M. Dehaan, M. Rivers, R. Wahls, Development of a Common Research Model for Applied CFD Validation Studies, 2008, https://doi.org/10.2514/6.2008-6919. URL: https://arc.aiaa.org/doi/abs/10.2514/6.2008-6919 https://arc.aiaa.org/doi/pdf/10.2514/6.2008-6919.
[124] NASA, NASA common research model, URL: https://commonresearchmodel.larc.nasa.gov/https://commonresearchmodel.larc.nasa.gov, 2020.
[125] M.B. Rivers, A. Dittberner, Experimental investigations of the NASA common research model, J. Aircraft 51 (2014) 1183–1193.
[126] M. Rivers, J. Quest, R. Rudnik, Comparison of the NASA common research model European transonic wind tunnel test data to NASA national transonic facility test data, CEAS Aeronautical J. 9 (2018) 307–317.
[127] M.B. Rivers, M. Lynde, R. Campbell, S. Viken, D. Chan, A.N. Watkins, S. Goodliff, Experimental investigation of the nasa common research model with a natural laminar flow wing in the nasa langley national transonic facility, in: AIAA Scitech 2019 Forum, American Institute of Aeronautics and Astronautics Inc, AIAA, 2019, https://doi.org/10.2514/6.2019-2189.
[128] M.N. Lynde, R.L. Campbell, M.B. Rivers, S.A. Viken, D.T. Chan, A.N. Watkins, S. L. Goodliff, Preliminary results from an experimental assessment of a natural laminar flow design method, in: AIAA Scitech 2019 Forum, American Institute of Aeronautics and Astronautics Inc, AIAA, 2019, https://doi.org/10.2514/6.2019-2298.
[129] S. Koga, M. Kohzai, M. Ueno, K. Nakakita, N. Sudani, Analysis of NASA common research model dynamic data in JAXA wind tunnel tests, in: 51st AIAA Aerospace Sciences Meeting Including the New Horizons Forum and Aerospace Exposition 2013, 2013, https://doi.org/10.2514/6.2013-495.
[130] R. Konrath, R. Geisler, J. Agocs, D. Otter, H. Ehlers, F. Philipp, J. Quest, High-speed PIV applied to wake of NASA CRM model in ETW under high re-number stall conditions for sub-and transonic speeds, in: 53rd AIAA Aerospace Sciences Meeting, American Institute of Aeronautics and Astronautics Inc, AIAA, 2015, https://doi.org/10.2514/6.2015-1095.
[131] T. Lutz, P.P. Gansel, J.L. Godard, A. Gorbushin, R. Konrath, J. Quest, S.M. B. Rivers, Going for experimental and numerical unsteady wake analyses combined with wall interference assessment by using the NASA CRM model in ETW, in: 51st AIAA Aerospace Sciences Meeting Including the New Horizons Forum and Aerospace Exposition 2013, 2013, https://doi.org/10.2514/6.2013-871.
[132] S. Koike, M. Ueno, Unsteady pressure measurement of transonic buffet on NASA common research model, in: 34th AIAA Applied Aerodynamics Conference, American Institute of Aeronautics and Astronautics Inc, AIAA, 2016, https://doi.org/10.2514/6.2016-4044.
[133] O. Brodersen, M. Rakowitz, S. Amant, P. Larrieu, D. Destarac, M. Sutcliffe, Airbus, ONERA, and DLR results from the 2nd AIAA drag prediction workshop, in: AIAA Paper, 2004, pp. 240–251, https://doi.org/10.2514/6.2004-391.
[134] E.N. Tinoco, O.P. Brodersen, S. Keye, K.R. Laflin, E. Feltrop, J.C. Vassberg, M. Mani, B. Rider, R.A. Wahls, J.H. Morrison, D. Hue, C.J. Roy, D.J. Mavriplis, M. Murayama, Summary data from the sixth AIAA CFD drag prediction workshop: CRM cases, J. Aircraft 55 (2018) 1352–1379.
[135] E.N. Tinoco, An Evaluation and Recommendations for Further CFD Research Based on the NASA Common Research Model (CRM) Analysis from the AIAA Drag Prediction Workshop (DPW) Series, Technical Report, Boeing Company and NASA, Seattle, WA, 2019. URL: https://ntrs.nasa.gov/search.jsp?R=20190027400.
[136] D. Hue, Q. Chanzy, S. Landier, DPW-6: drag analyses and increments using different geometries of the common research model airliner, J. Aircraft 55 (2018) 1509–1521.
[137] NASA, Turbulence modeling resource, URL: https://turbmodels.larc.nasa.gov/, 2020.
[138] T. Zhaoguang, C. Yingchun, S. Jiangtao, Study of power influences to the wing-mounted civil aircraft aerodynamic characteristics, J. Aircraft 51 (2014) 629–636.
[139] D. Berry, The boeing 777 engine/airframe integration aerodynamic design process, in: ICAS 1994, ICAS, Anaheim, USA, 1994, pp. 1305–1320. URL: https://www.icas.org/ICAS{_}ARCHIVE/ICAS1994/ICAS-94-6.4.4.pdf.
[140] T. Sibilli, M. Savill, V. Sethi, D. MacManus, A.M. Rolt, Numerical simulation of propulsion system integration for very high bypass ratio engines, in: Volume 1: Aircraft Engine; Ceramics; Coal, Biomass and Alternative Fuels; Controls, Diagnostics and Instrumentation, American Society of Mechanical Engineers, 2012, pp. 185–193, https://doi.org/10.1115/GT2012-68908. URL: https://asmedigitalcollection.asme.org/GT/proceedings/GT2012/44670/185/289193.
[141] T.P. Stánkowski, D.G. MacManus, C.T. Sheaf, R. Christie, Aerodynamics of aero-engine installation, Proc. IME G J. Aero. Eng. 230 (2016) 2673–2692.
[142] T.P. Stańkowski, D.G. MacManus, C.T. Sheaf, R. Christie, Aerodynamics of aero-engine installation, Proc. IME G J. Aero. Eng. 230 (2016) 2673–2692.
[143] J.J. Otter, T. Stańkowski, M. Robinson, D.G. MacManus, Installation aerodynamics of civil aero-engine exhaust systems, Aero. Sci. Technol. 89 (2019) 345–355.
[144] S. Ritter, Impact of different UHBR-engine positions on the aerodynamics of a high-liftwing, Notes on Num. Fluid Mech. Multidisciplinary Des. 131 (2016) 367–380.
[145] S. Koc, H.J. Kim, K. Nakahashi, Aerodynamic design of wing-body-nacelle-pylon configuration, in: 17th AIAA Computational Fluid Dynamics Conference, American Institute of Aeronautics and Astronautics, Reston, Viriginia, 2005, https://doi.org/10.2514/6.2005-4856. URL: http://arc.aiaa.org/doi/10.2514/6.2005-4856.
[146] S.C. Smith, M. Nemec, S.E. Krist, Integrated nacelle-wing shape optimization for an Ultra- High Bypass fanjet installation on a single-aisle transport configuration, in: 51st AIAA Aerospace Sciences Meeting Including the New Horizons Forum and Aerospace Exposition 2013, American Institute of Aeronautics and Astronautics, Reston, Viriginia, 2013, https://doi.org/10.2514/6.2013-543. URL: http://arc.aiaa.org/doi/10.2514/6.2013-543.
[147] J. Li, Z. Gao, J. Huang, K. Zhao, Aerodynamic design optimization of nacelle/pylon position on an aircraft, Chin. J. Aeronaut. 26 (2013) 850–857.
[148] B. Epstein, S. Peigin, Automatic optimization of wing–body–under-the-wing-mounted-nacelle configurations, J. Aircraft 53 (2016) 691–700.
[149] R. Lei, J. Bai, D. Xu, Aerodynamic optimization of civil aircraft with wing-mounted engine jet based on adjoint method, Aero. Sci. Technol. 93 (2019), 105285.
[150] J.R. Hooker, A. Wick, C. Zeune, A. Agelastos, Over wing nacelle installations for improved energy efficiency, in: 31st AIAA Applied Aerodynamics Conference, American Institute of Aeronautics and Astronautics, Reston, Virginia, 2013, https://doi.org/10.2514/6.2013-2920. URL: http://arc.aiaa.org/doi/10.2514/6.2013-2920.
[151] L. Savoni, R. Rudnik, Pylon design for a short range transport aircraft with over-the-wing mounted uhbr engines, in: AIAA Aerospace Sciences Meeting, 2018, American Institute of Aeronautics and Astronautics Inc, AIAA, 2018, p. 210059, https://doi.org/10.2514/6.2018-0011.
[152] C. Sabater Campomanes, External Flow Effects in the Engine/Airframe Integration Testing Technique, Msc thesis, Delft University of Technology, 2017. URL: https://repository.tudelft.nl/islandora/object/uuid{%}3Ae9e66768-b0be-49f0-970a-1a9adf41a377.
[153] W. de Wolf, Possibilities and Limitations of VHBR and UHBPR Turbofan Simulations in Engine/Airframe Integration Wind Tunnel Experiments, Technical Report, NLR, Braunschweig, 1996.
[154] M. Laban, B. Soemarwoto, J. Kooi, Reshaping Engine Nacelles for Testing in Wind Tunnels with Turbofan Propulsion Simulators, American Institute of Aeronautics and Astronautics (AIAA), 2005, https://doi.org/10.2514/6.2005-3703.
[155] H. Geyr, C. Rossow, A correct thrust determination method for turbine powered simulators in wind tunnel testing, in: 41st AIAA/ASME/SAE/ASEE Joint Propulsion Conference & Exhibit, American Institute of Aeronautics and Astronautics, Reston, Viriginia, 2005, https://doi.org/10.2514/6.2005-3707. URL: http://arc.aiaa.org/doi/abs/10.2514/6.2005-3707.
[156] A.E. Harris, J.T. Kutney, F.B. Ogilvie, 25 years of turbine powered simulation succes, in: International Forum on Turbine Powered Simulation, International Forum on Turbine Powered Simulation, 1995.
[157] D. Eckert, V.v. Ditshuizen, B. Munniksma, W. Burgsmuller, Low speed twin engine simulation on a large scale transport aircraft model in the dnw, in: International Counsil of the Aeronautical Sciences, International Counsil of the Aeronautical Sciences, 1982.
[158] J.W. Kooi, N. Corby, G.H. Hegen, Tps Calibration Procedures, 1995.
[159] J.W. Kooi, L.d. Haij, G.H. Hegen, Engine simulation with turbofan propulsion simulators in the German-Dutch wind tunnels, URL: https://arc.aiaa.org/doi/abs/10.2514/6.2002-2919, 2002 https://arc.aiaa.org/doi/pdf/10.2514/6.2002-2919.
[160] R. Decher, D. Tegeler, High accuracy force accounting procedures for turbopowered simulator testing, URL: https://arc.aiaa.org/doi/abs/10.2514/6.1975-1324, 1975 https://arc.aiaa.org/doi/pdf/10.2514/6.1975-1324.

[161] H. Hoheisel, H. Frhr, von Geyr, The influence of engine thrust behaviour on the aerodynamics of engine airframe integration, CEAS Aeronautical J. 3 (2012).
[162] W. Burgsmuller, C. Castan, H. Hoheisel, J.W. Kooi, Preparation and use of tps-technique for low-speed investigations on transport aircraft, Proceedings of the International Forum on Turbine Powered Simulation at DNW (1995) 34–42.
[163] G.W. Hall, Application of boundary layer theory to explain some nozzle and venturi flow peculiarities, Proc. Inst. Mech. Eng. 173 (1959) 837–870.
[164] K. Mikkelsen, R. Brasket, An equation set for ASME nozzle discharge and thrust coefficients, URL: https://arc.aiaa.org/doi/abs/10.2514/6.2011-1265, 2011 https://arc.aiaa.org/doi/pdf/10.2514/6.2011-1265.
[165] K. Mikkelsen, D. Myren, D. Dahl, M. Christiansen, Initial subscale performance measurements of the AIAA dual separate flow reference (DSFR) nozzle, URL: https://arc.aiaa.org/doi/abs/10.2514/6.2015-3883, 2015 https://arc.aiaa.org/doi/pdf/10.2514/6.2015-3883.
[166] F. Wright, Comparison of least squares curve fit and individual sample statistical analysis results of calibration data for the velocity coefficient of a flow nacelle, URL: https://arc.aiaa.org/doi/abs/10.2514/6.1994-2587, 1994 https://arc.aiaa.org/doi/pdf/10.2514/6.1994-2587.
[167] D. Yoder, V. Dippold, N. Georgiadis, Wind-us Results for the Aiaa 1st Propulsion Aerodynamics Workshop, AIAA 1st Propulsion Aerodynamics Workshop, 2012.
[168] V. Dippold, L. Foster, M. Mankbadi, Wind-us Results for the Aiaa 2nd Propulsion Aerodynamics Workshop, AIAA 2nd Propulsion Aerodynamics Workshop, 2014.
[169] R.L. Thornock, E.F. Brown, An experimental study of compressible flow through convergent-conical nozzles, including a comparison with theoretical results, J. Basic Eng. 94 (1972) 926–930.
[170] J.E. McCall, P. Tracksdorf, K. Heinig, Advanced ducted engine nacelle aerodynamics and integration testing, J. Eng. Gas Turbines Power 114 (1992) 802–808.
[171] G. Doornbos, W.d. Wolf, The Engine/airframe Interference Drag at Cruise Conditions, Using Propulsion Simulation, NLR, Marknesse, 1983. Technical Report NLR TR 82012 U.
[172] D.M. Tompkins, J.D. Flamm, K.R. Long, K.D. James, Experimental validation of modifications to a TDI model 2700 turbine powered simulator to simulate a high-bypass ratio engine, URL: https://arc.aiaa.org/doi/abs/10.2514/6.2014-3888, 2014 https://arc.aiaa.org/doi/pdf/10.2514/6.2014-3888.
[173] H.R. Welge, J.R. Ongarato, Powered -engine simulator procedures and experience for the dc-10 wing engine, J. Aircraft 8 (1971) 523–529.
[174] P.R. Shea, J.D. Flamm, K. Long, K.D. James, D. Tompkins, M.D. Beyar, Turbine powered simulator calibration and testing for hybrid wing body powered airframe integration (invited), URL: https://arc.aiaa.org/doi/abs/10.2514/6.2016-0011, 2016 https://arc.aiaa.org/doi/pdf/10.2514/6.2016-0011.
[175] E.D. Dickey, N. Princen, J.T. Bonet, G.K. Ige, Wind tunnel model design and fabrication of a 5.75% scale blended-wing-body twin jet configuration (invited), URL: https://arc.aiaa.org/doi/abs/10.2514/6.2016-0008, 2016 https://arc.aiaa.org/doi/pdf/10.2514/6.2016-0008.